Check for updates

Global chemical weathering dominated by continental arcs since the mid-Palaeozoic

Thomas M. Gernon [1] ✉, Thea K. Hincks[1], Andrew S. Merdith [2,3], Eelco J. Rohling [1,4], Martin R. Palmer[1], Gavin L. Foster[1], Clément P. Bataille[5] and R. Dietmar Müller [6]

Earth's plate-tectonic activity regulates the carbon cycle and, hence, climate, via volcanic outgassing and silicate-rock weathering. Mountain building, arc–continent collisions and clustering of continents in the tropics have all been invoked as controlling the weathering flux, with arcs also acting as a major contributor of carbon dioxide to the atmosphere. However, these processes have largely been considered in isolation when in reality they are all tightly coupled. To properly account for interactions among these processes, and the inherent multi-million-year time lags at play in the Earth system, we need to characterize their complex interdependencies. Here we analyse these interdependencies over the past 400 million years using a Bayesian network to identify primary relationships, time lags and drivers of the global chemical weathering signal. We find that the length of continental volcanic arcs—the fastest-eroding surface features on Earth—exerts the strongest control on global chemical weathering fluxes. We propose that the rapid drawdown of carbon dioxide tied to arc weathering stabilizes surface temperatures over geological time, contrary to the widely held view that this stability is achieved mainly by a delicate balance between weathering of the seafloor and the continental interiors.

Weathering of Earth's surface regulates climate over geological timescales (~1–10 Myr)[1–5]. When atmospheric carbon dioxide (CO_2) concentrations are high and temperatures elevated, these conditions lead to ocean acidification and an intensified hydrologic cycle with increased evaporation, precipitation and runoff[1]. These conditions give rise to enhanced weathering of silicate minerals and CO_2 drawdown. Conversely, reduced silicate weathering reduces CO_2 drawdown under cold climates, promoting warming. This 'thermostat' stabilizes surface temperatures through time[6]. During the Phanerozoic eon (541–0 million years ago (Ma)), the periodic onset of icehouse conditions has variously been attributed to enhanced weathering rates associated with mountain building[4,7], reductions in continental arc magmatism[8] and uplift of oceanic crust during arc–continent collisions[9]. Rather than occurring in isolation, these global tectonic processes are inextricably linked, and the resulting collinearity—coupled with unknown time lags—obscures each process's individual contribution to global weathering fluxes. These issues have thus far severely limited our understanding of the first-order drivers of Earth's weathering fluxes.

Deep-time data mining

To address this problem, we constructed a deep-time Bayesian network (BN), a class of probabilistic graphical model that represents a set of variables (nodes) and their conditional dependencies (Methods). This approach—widely applied in machine learning—can be used to quantify the strength of influence of individual processes on an outcome of interest (for example, a chemical signal in seawater). Our BN uses data mining to systematically quantify the strength of the relationships between key geological variables and the chemical weathering flux to identify primary drivers and lags. To perform the analysis, we use UNINET, a software package for uncertainty analysis and high dimensional-dependence mod-

elling. UNINET has proven capability for analysing complex data and evaluating geological relationships and temporal dependencies[10]. We focus on the past 400 Myr, when key predictors of weathering flux such as crustal distribution, seafloor production rates[11] and atmospheric CO_2[12] are generally well constrained (Fig. 1). This period was also chosen because (1) it captures the assembly and breakup of the supercontinent Pangaea (Fig. 1a), stable from ~320 to 200 Ma (Fig. 1f), and (2) the four main lineages of vascular plants had already proliferated on land by 400 Ma[13], meaning we do not expect the interval to encompass a step change in terrestrial weathering tied to soil–plant biogeochemical cycles. We compiled geospatial datasets using palaeogeographic reconstruction from the open-source plate-tectonic software GPlates[14], processed in R (Methods), to produce a diverse set of time series that capture times of key global tectonic changes (Fig. 1). Parameters include continental arc length[15], climate state (characterized by latitudinal extent of continental ice[9] and atmospheric CO_2 concentration[12]), suture-zone length as a proxy for arc–continent collisions[9], the spatial extent of large igneous provinces (LIPs)[16], seafloor production rates, and continental fragmentation and dispersal (Fig. 1a,f).

We used variations in strontium isotope ratios in seawater (($^{87}Sr/^{86}Sr)_{sw}$) derived from marine carbonates[17] as a proxy for global chemical weathering through time and calculated a moving average using a ± 0.25 Myr window (Fig. 1g). Given the large contrast in $^{87}Sr/^{86}Sr$ between radiogenic continents and unradiogenic oceanic crust[18], ($^{87}Sr/^{86}Sr)_{sw}$ is thought to represent a globally integrated balance in weathering flux from continental surfaces and the seafloor[17–19]. We tested this assertion by constructing a network to explore the relationship between ($^{87}Sr/^{86}Sr)_{sw}$ and partial pressure of atmospheric carbon dioxide (p_{CO_2}) since 400 Ma[12]. This analysis reveals a clear relationship between ($^{87}Sr/^{86}Sr)_{sw}$ and p_{CO_2} (empirical correlation = −0.57) at lag zero, which decreases with increasing

[1]School of Ocean and Earth Science, University of Southampton, Southampton, UK. [2]Laboratoire de Géologie, Université of Lyon 1, Lyon, France. [3]School of Earth and Environment, University of Leeds, Leeds, UK. [4]Research School of Earth Sciences, The Australian National University, Canberra, Australian Capital Territory, Australia. [5]Earth and Environmental Sciences, University of Ottawa, Ottawa, Ontario, Canada. [6]EarthByte Group, School of Geosciences, The University of Sydney, Sydney, New South Wales, Australia. ✉e-mail: Thomas.Gernon@noc.soton.ac.uk

lags (Extended Data Fig. 1), confirming they are coupled[4]. However, as there are clearly secondary controls on $(^{87}Sr/^{86}Sr)_{sw}$ and some uncertainty in the CO_2 record used[12], the relationship is not straightforward; this is a key justification for analysing what drives these variations through time. We present our results in terms of $(^{87}Sr/^{86}Sr)_{sw}$—the standard framework—but also test the sensitivity of our model to radioactive decay of ^{87}Rb (to ^{87}Sr) in the crust through time[20].

Building an Earth network

Despite progress in linking variations in $(^{87}Sr/^{86}Sr)_{sw}$ to geodynamic and palaeogeographic factors[21], it is unclear how processes combine to drive $(^{87}Sr/^{86}Sr)_{sw}$ variations. We constructed the network (Methods) with nodes for $(^{87}Sr/^{86}Sr)_{sw}$ and 12 predictor variables (Extended Data Fig. 2 and Supplementary Data 1), with lags from 0 to 50 Myr. We present three correlation measures that summarize the relationships between the variables and $(^{87}Sr/^{86}Sr)_{sw}$ (Figs. 2–4). First, the empirical rank correlation (C_{Emp}, the Spearman rank correlation) is a non-parametric measure of the relationship between two variables. Although informative, this does not account for autocorrelation or the joint influence of other variables. Second, the BN rank correlation (C_{BN}) is the modelled representation of the empirical rank correlation. In an ideal case (a perfect model), this would be equal to C_{Emp}. Third, the conditional rank correlation (C_{Cond}) is the rank correlation between two variables conditional on any other parent variables (accounting for the effect of all nodes at shorter lags and higher up in the network hierarchy; Methods).

We construct our network by starting with the variable with the highest empirical rank correlation with $(^{87}Sr/^{86}Sr)_{sw}$ at lag zero and systematically search the set of predictor variables to find maximum values of C_{Cond} at increasing lags (each 2.5 Myr window) up to 50 Myr (Methods). A variable is added to the network if its conditional correlation exceeds a confidence interval threshold (dependent on the number of original data points). The conditional correlation removes the influence of variables higher in the network hierarchy (and at shorter lags) and provides a measure of the additional information each subsequent lagged variable provides in explaining $(^{87}Sr/^{86}Sr)_{sw}$ variation (Fig. 4 and Extended Data Figs. 3 and 4). This approach is based on the method for partial autocorrelation and efficiently accounts for multiple joint dependencies and lags (Methods). While our focus in the following account is on C_{Cond}, for context we also provide C_{Emp} and C_{BN} (Fig. 4 and Extended Data Table 1).

Identification of chemical weathering drivers

We find that the length of continental volcanic arcs[15] (Fig. 1c), where oceanic lithosphere is subducted beneath continental lithosphere[8], is most strongly correlated with $(^{87}Sr/^{86}Sr)_{sw}$ ($C_{Emp} = -0.79$; $C_{Cond} = -0.70$; Figs. 2, 3a, 4a), increasing when we correct for crustal radioactive decay of ^{87}Rb (ref. [20]; $C_{Emp} = -0.82$; Fig. 2 and Extended Data Table 2). This strong relationship (Figs. 2, 3a) suggests that periods of increased continental arc volcanism have favoured unradiogenic seawater compositions, and vice versa. Today, the global continental arc system is ~14,000 km long[15] and includes regions such as the Alaska Peninsula, the Cascades and the Andean Volcanic Belt (Extended Data Fig. 5). The global arc system was three times longer (~37,500 km) during the Mesozoic (Fig. 1c),

reflecting a sharp increase in seafloor production (Figs. 1c–d). The ocean chemical response to changing arc extent is rapid, peaking in <0.5 Myr (Fig. 4a). Before exploring the importance of these observations, we need to quantitatively evaluate how other processes combine to drive $(^{87}Sr/^{86}Sr)_{sw}$.

Terrestrial weathering fluxes are highly sensitive to crustal deformation[1,4–7]. It has been suggested that arc–continent collisions in the tropics—where volcanic island arcs are obducted onto continents forming ophiolite complexes—gave rise to enhanced weathering of (ultra-) mafic lithologies and CO_2 drawdown, driving Phanerozoic glaciations[9,22]. Weathering of ultramafic lithologies on this scale should reduce $(^{87}Sr/^{86}Sr)_{sw}$, so the correlation should be negative, reflecting unradiogenic inputs to oceans. To evaluate this, we incorporate suture-length data[9] into our network (Fig. 1e and Extended Data Fig. 6). The empirical correlation between active suture length and $(^{87}Sr/^{86}Sr)_{sw}$ is strong and positive. Accounting for other dominant processes (continental arc length), this reduces, leaving a peak $C_{Cond} = 0.47$ at lag zero (Fig. 4b). Given that we find consistently positive correlations between suture length and $(^{87}Sr/^{86}Sr)_{sw}$ (Fig. 4b), we infer that arc–continent collisions promote enhanced weathering of radiogenic continental material via orogenesis and erosion[4,7], rather than predominantly unradiogenic ultramafics as suggested before[9,22]. Our results are consistent with the conventional uplift–weathering hypothesis[4] and help explain the reported link between arc–continent collisions and glaciations[9]. Increasing suture length appears to drive enhanced weathering of continental material, promoting CO_2 consumption and cooling.

Chemical weathering is also sensitive to continental fragmentation, which increases the reach of oceanic moisture into continental interiors[23], but the timescales and impacts are highly uncertain. To address this, we consider geospatial attributes of continents through time (Methods). Using the footprint defined by continent–ocean boundaries[11], we computed the continental perimeter/area ratio[24,25]—a quantitative measure of crustal fragmentation (Fig. 1f). We find that the correlation between continental fragmentation and $(^{87}Sr/^{86}Sr)_{sw}$ is moderate to low (maximum $C_{Cond} = 0.31$) and positive, consistent with enhanced weathering of radiogenic crust during plate-tectonic fragmentation. The peak C_{Cond} at time lags of ~12.5–15 Myr (Fig. 4c) is commensurate with typical timescales of rift-to-drift transitions and delayed basin connectivity following continental breakup[26]. Accounting for lags of this order will be crucial to correct interpretation of associations between tectonic fragmentation and marine biodiversity[27].

High temperatures and precipitation usually favour high weathering rates in tropical regions[9,23]. It has thus been hypothesized that a high proportion of continental land masses within the tropics could strongly influence global weathering[23]. We test this by quantifying continental area within the tropical latitudinal bands (we test both ±20° and ±10° of the equator) at intervals of 1 Myr (Fig. 1f and Extended Data Fig. 7) and integrate this in our network. The land surface area within the tropics has increased over 400–0 Ma (Fig. 1f) but makes a negligible contribution to weathering fluxes from the continental surface (Extended Data Fig. 3). This could be due to development of deep, indurated soil profiles in tropical drainage basins that lead to very low (transport-limited) weathering intensity[28]. Similarly, the spatial

Fig. 1 | Tectonic, atmospheric and ocean chemical changes over the past 410 Myr. a, Continental distribution[11] with continental land masses shown in pink, present-day coastlines in black, and the tropics (±20° of the Equator) in beige. **b**, Atmospheric CO_2 concentration (multi-proxy, black line)[12] and phytane-based estimates (in red)[50]; continental-ice latitude[9] is represented by the blue line (blue-shaded regions denote glaciations). **c**, Continental arc length[15]. **d**, Seafloor production rates (Methods). **e**, Suture-zone length[9]. **f**, Fragmentation index (continental perimeter/area, as black line) and total area of continents in the tropics (red line). **g**, $(^{87}Sr/^{86}Sr)_{sw}$ from marine carbonates[17], calculated as a ±0.25 Myr window (in red). **h**, Normalized $(^{87}Sr/^{86}Sr)_{sw}$ curve removing the signal caused by radioactive ^{87}Rb decay in the crust[20]. Minimum and maximum estimated uncertainties are shown in grey (and pink in **f**); for all time series used and their uncertainty distributions, see Extended Data Fig. 2 and Supplementary Data 1.

extent of LIPs through time[16] is only very weakly related to $(^{87}Sr/^{86}Sr)_{sw}$ (Extended Data Fig. 3), possibly because they are typically flat-lying rather than mountainous terrains. This suggests that environmental perturbations associated with LIPs are probably due to changes in volcanic CO_2 fluxes[29] rather than enhanced weathering of mafic lithologies.
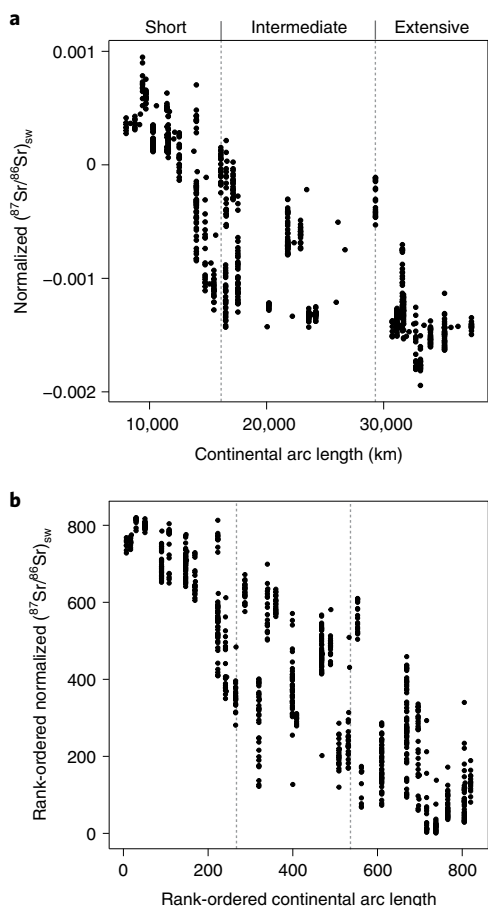
a Short | Intermediate | Extensive

b
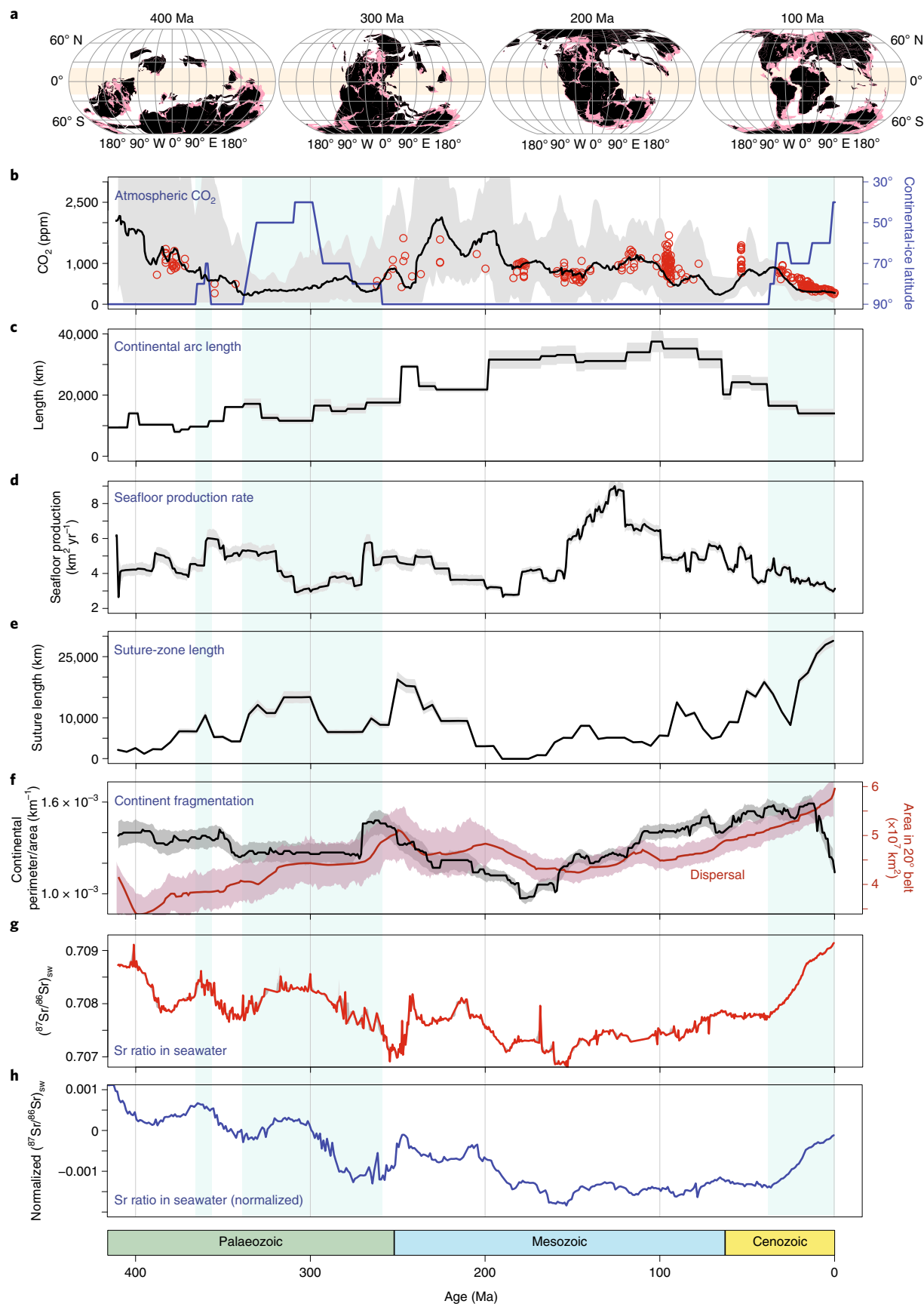
Fig. 2 | Effects of continental arc extent on the strontium isotopic composition of seawater. a, Normalized $(^{87}Sr/^{86}Sr)_{sw}$ (using ref.[20]) versus continental arc length; the dashed vertical lines show the divisions between short (<16,100 km), intermediate (16,100–29,300 km) and extensive (≥29,300 km) arc systems (these divisions denote approximately equal quantiles). **b**, Ranked normalized $(^{87}Sr/^{86}Sr)_{sw}$ versus ranked continental arc length; note that the smallest value that occurs in the dataset is ranked 1. The ranked plot is a particularly useful way to visualize the relationship between variables because it shows the correlation of the non-parametric form of the data; it is less sensitive to the underlying distributions of the data being analysed or the effects of any extreme outliers.

It is well established that seafloor basalt alteration[30] and hydrothermal venting decrease $(^{87}Sr/^{86}Sr)_{sw}$ (towards mid-ocean-ridge-basalt mantle $^{87}Sr/^{86}Sr \simeq 0.7035$; ref.[19]). Therefore, $(^{87}Sr/^{86}Sr)_{sw}$ is expected to scale inversely with seafloor production rate (Fig. 1d), which we calculate as the product of ridge length and spreading rate (Extended Data Fig. 8), adapting an existing plate model[25]. We find that seafloor production rates are negatively correlated with $(^{87}Sr/^{86}Sr)_{sw}$ at short lags (Fig. 4d), reflecting the effects of early high-temperature alteration of basalts along ridge axes[31]. The seafloor weathering contribution becomes negligible ~15–20 Myr after emplacement, suggesting that seafloor is not releasing unradiogenic Sr appreciably after this time. This is strikingly consistent with hydrothermal models[32] and observations of secondary minerals in ocean crust[33,34], which indicate that ~70–80% of fluid flux occurs in seafloor within 20 Myr of formation. We find that radiogenic continental weathering sources dominate the $(^{87}Sr/^{86}Sr)_{sw}$ signal at lags >20 Myr, explaining the switch to a positive correlation (Fig. 4d).

Glacial intensity is also known to influence $(^{87}Sr/^{86}Sr)_{sw}$[35]. Investigating the effect of continental-ice coverage, we find a
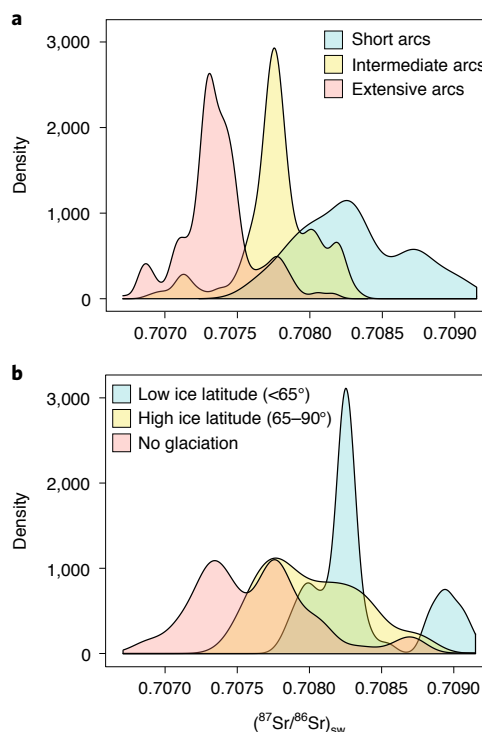

a

b

Fig. 3 | Effects of continental arc extent and global ice distribution on the strontium isotopic composition of seawater. a, Probability density for continental arc length[15], identifying short (<16,100 km), intermediate (16,100–29,300 km) and extensive (≥29,300 km) arcs (note: these divisions denote approximately equal quantiles); the distributions show that extensive continental arc systems favour low $(^{87}Sr/^{86}Sr)_{sw}$ and vice versa. **b**, Probability density for latitudinal ice extent, showing the $(^{87}Sr/^{86}Sr)_{sw}$ during periods of low ice latitude (<65°), high ice latitude (65–90°) and no glaciation (90°). The distributions show that more extensive (severe) glaciations favour high $(^{87}Sr/^{86}Sr)_{sw}$ and vice versa.

strong empirical correlation between latitudinal extent of ice sheets (Fig. 1b) (as a proxy for the severity of glaciation and global climate[9]) and $(^{87}Sr/^{86}Sr)_{sw}$ (−0.72; Figs. 3b, and 4e), supporting the notion that glaciations cause intensified weathering of continental crust[18,35–37]. This is probably due to preferential weathering of radiogenic minerals such as biotite in comminuted rock flour characteristic of glaciated catchments[36,37]. The conditional correlation is low due to collinearity between the ice extent and the arc and suture lengths. Observations suggest that weathering influences atmospheric CO_2 concentration[12] (Fig. 1f and Extended Data Fig. 1) but also provide evidence for a feedback whereby CO_2 influences weathering (negative $C_{Emp} = -0.58$ where $(^{87}Sr/^{86}Sr)_{sw}$ lags CO_2 by 0.5–2.5 Myr, in Fig. 4f). A weak, but statistically significant positive C_{Cond} between CO_2 and $(^{87}Sr/^{86}Sr)_{sw}$ at lags >10 Myr (Fig. 4f and Extended Data Figs. 3f and 4f) suggests a weak negative carbonate–silicate feedback operating over tens of millions of years. This appears to be a secondary effect.

Unpicking uncertainty

To determine how input uncertainties could affect results, we simulated 1,000 variant time series for each input parameter and repeated the BN analysis using this alternative input dataset (Methods). Where available, we used existing uncertainty estimates (for example, for p_{CO_2} and continental arc length) and simulated uncertainty for other key variables using the best existing knowledge (Extended Data Fig. 2). The analysis reveals that when uncertainty envelopes are considered, the strongest correlations with $(^{87}Sr/^{86}Sr)_{sw}$ remain
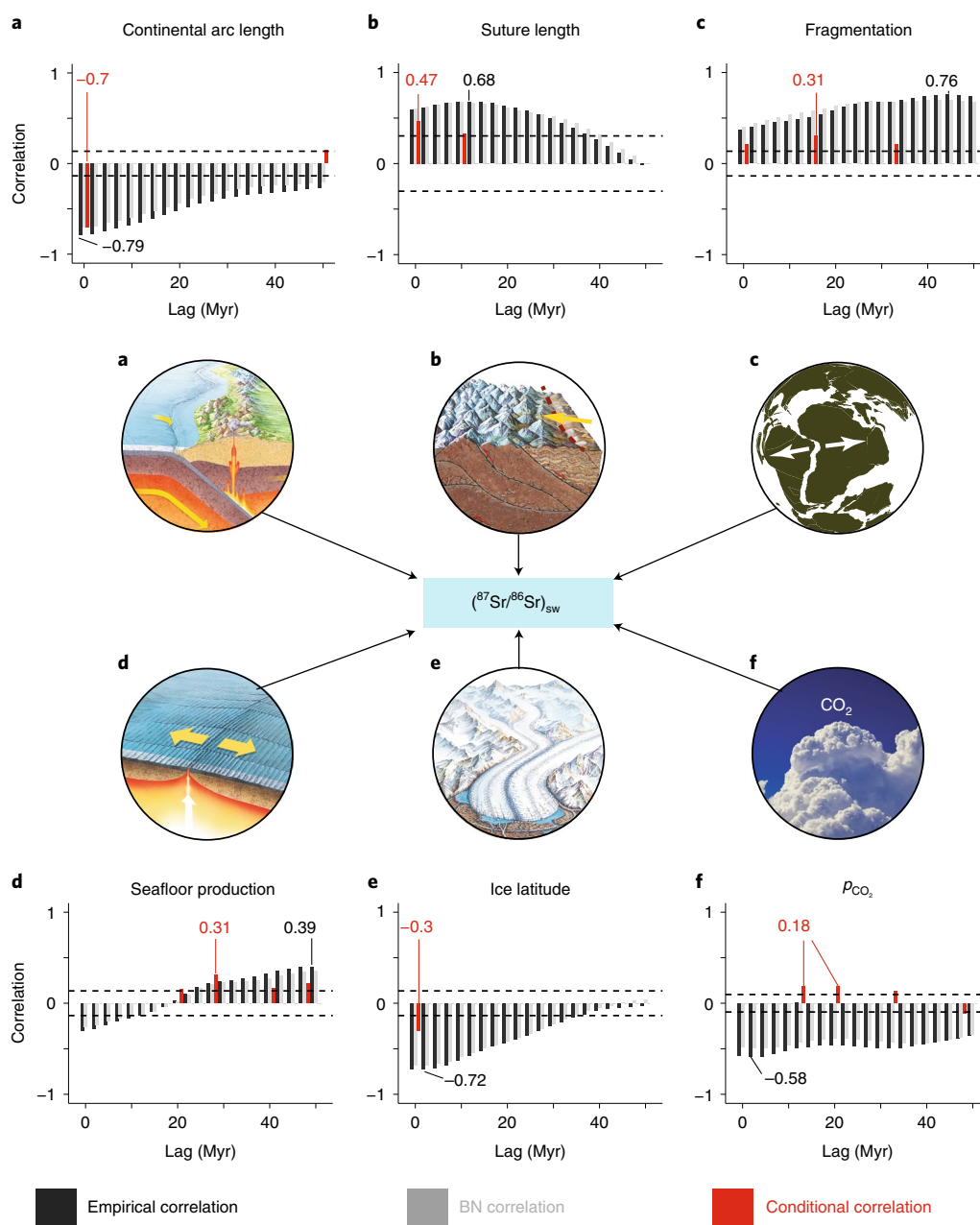
Fig. 4 | Simplified network showing key geological processes and correlations with seawater Sr. a–f, Illustration of a subset of our network, showing how six key variables (continental arc length (**a**), suture length (**b**), fragmentation (**c**), seafloor production (**d**), ice latitude (**e**) and p_{CO_2} (**f**)) influence or lead $({}^{87}Sr/{}^{86}Sr)_{sw}$ (Extended Data Fig. 3). The plots summarize the relationships between each variable and $({}^{87}Sr/{}^{86}Sr)_{sw}$ using regular 0.5 Myr time series, spanning the period 410 Ma to 0.5 Ma ($n = 720$ time steps after accounting for lags). C_{Emp}, C_{BN} and C_{Cond} are computed at lags from 0 to 50 Myr in 2.5 Myr intervals. A lag of zero means the processes occur within the same 0.5 Myr time step. The numbers in black denote the highest absolute values of C_{Emp}; if each process were considered in isolation, this value could be interpreted as the dominant time lag. However, due to autocorrelation and joint dependence, the key drivers and their associated lags can be better identified by peak C_{Cond} (red). The horizontal dashed lines denote 99% confidence intervals estimated from the number of original data points for a given variable.

largely unchanged (Extended Data Figs. 3 and 4), with very small differences between the BN and empirical correlations for the original and variant inputs (Extended Data Table 1 and Supplementary Data 3).

Central role for volcanic arc weathering

This analysis supports our overall conclusion that continental volcanic arc length exerts the strongest influence on global weathering fluxes during greenhouse intervals. This is consistent with regional studies[38,39] and the observation that chemical weathering

of island arcs dominates the oceanic Sr budget today[40] and may even have contributed to Neogene cooling[41]. We might expect that the variation of the island-arc source over time would be similar to the continental arc source because both are ultimately dependent on spreading rates. However, we do not have a sufficiently extensive or accurate record of island-arc lengths to test this hypothesis. However, if we assume that the global length of subduction zones is a crude proxy for oceanic island-arc length, the observed relatively weak conditional correlations (Extended Data Fig. 3g) suggest that volcanic island arcs are unlikely to be a first-order driver of the

weathering signal over geological timescales in contrast to continental arcs. The latter are an important contributor to the atmospheric CO_2 inventory, owing to a propensity for decarbonation reactions in the continental lithosphere[8]. The strongly negative correlation between continental arc length and $(^{87}Sr/^{86}Sr)_{sw}$ (Figs. 2, 3a and 4a) is consistent with the hypothesis that their formation and spatial extent govern icehouse–greenhouse transitions[8].

The high CO_2 outgassing flux and greenhouse conditions associated with extensive continental arcs[8] favour intensified chemical weathering[1,5,6]. Today, continental volcanic arcs are among the highest topographic—and fastest-eroding—surface features on Earth[38], supplying Ca–Mg silicate weathering products to the ocean over tens of millions of years[39]. Hydrothermal activity maximizes water–rock interactions, which, given the enhanced orographic precipitation typical in these regions, results in extreme chemical denudation rates[42,43]. For example, the present-day Andes (Extended Data Fig. 5) dominates dissolved ion fluxes to the Amazon River[44], fuelling Earth's greatest offshore river plume. Today, continental arcs are predominantly unradiogenic (Extended Data Fig. 5), with mean $^{87}Sr/^{86}Sr$ values of 0.7044 ($N= 5{,}498$; median $= 0.704$, mode $= 0.7035$), only slightly higher than typical mid-ocean-ridge basalts and ocean island basalts[45]. Thus, prolonged cycles of arc assembly, erosion and weathering[38,39] probably drove seawater towards the unradiogenic compositions we observe (Figs. 2–4). Greenhouse conditions linked to extensive arcs[8] should promote increased bottom-water temperatures and enhanced seafloor weathering[46], further reducing $(^{87}Sr/^{86}Sr)_{sw}$.

Continental volcanic arcs are predisposed to acid-intermediate magmatism, favouring zircon production[47]. The interpretation that continental arcs drive global chemical weathering fluxes (Fig. 2) is therefore consistent with an observed increase in detrital zircon abundance during greenhouse intervals[8]. The latter implicates increased transport and weathering of arc detritus to ocean basins when continental arcs are longest. Our analysis confirms that the $^{87}Sr/^{86}Sr$ of zircon-bearing igneous rocks strongly correlates with $(^{87}Sr/^{86}Sr)_{sw}$ over the past 400 Myr (Extended Data Table 2), suggesting that global chemical weathering is tightly coupled to the composition of continental igneous lithologies[20]. The correlation between igneous $^{87}Sr/^{86}Sr$ and $(^{87}Sr/^{86}Sr)_{sw}$ is highest[20] when arc systems are longest[15]. It is therefore probable that the length of continental arcs drives $(^{87}Sr/^{86}Sr)_{sw}$ via the proportional availability of weatherable igneous catchments. This finding draws specific attention to the rock compositions (calc–alkaline) and climate conditions (predominantly highland and tropical–humid) that offer the best potential for accelerated CO_2 drawdown in enhanced weathering schemes designed to counteract current global climate change[48].

To summarize, we have developed a data-mining approach based on conditional probability estimation to disentangle complex interdependencies among solid Earth, hydrosphere and atmospheric processes over the past 400 Myr. This approach offers considerable potential to aid interpretation of complex Earth data that exhibits high dimensional dependency on different spatial and temporal scales.

It is widely accepted that continental arcs modulate atmospheric CO_2 levels[8,49] and represent a major agent of crustal growth through post-Archaean Earth history via arc accretion processes[38]. Our analysis indicates that arcs have also dominated global chemical weathering fluxes, which determine the Sr isotopic composition of seawater, $(^{87}Sr/^{86}Sr)_{sw}$, over the past 400 Myr. This revises conventional concepts that $(^{87}Sr/^{86}Sr)_{sw}$ is driven by competition between weathering of the seafloor and continental interiors. Arc weathering causes reduction in $(^{87}Sr/^{86}Sr)_{sw}$ while continental weathering causes increases in $(^{87}Sr/^{86}Sr)_{sw}$. Thus, our findings of arc dominance in weathering help explain enigmatic low $(^{87}Sr/^{86}Sr)_{sw}$ during greenhouse climates, where the higher temperatures should, according to conventional concepts, have promoted greater continental crust weathering[6], driving increased $(^{87}Sr/^{86}Sr)_{sw}$.

Our results indicate that continental arcs provide a self-regulating thermostat, gradually removing atmospheric CO_2 via rock-weathering reactions that offset their more rapid high volcanic CO_2 outgassing fluxes. Conversely, when continental arc extent reduces, global CO_2 emissions decrease, arc weathering slows and continental-ice sheets become the principal agent of physical and chemical weathering, driving increased $(^{87}Sr/^{86}Sr)_{sw}$. Through this regulation of atmospheric CO_2 levels over geological timescales, continental volcanic arcs played a central role in maintaining habitability over the course of Earth history even in the face of dramatic external drivers.

Online content

Any methods, additional references, Nature Research reporting summaries, source data, extended data, supplementary information, acknowledgements, peer review information; details of author contributions and competing interests; and statements of data and code availability are available at https://doi.org/10.1038/s41561-021-00806-0.

References

1. Kump, L. R., Brantley, S. L. & Arthur, M. A. Chemical weathering, atmospheric CO_2, and climate. *Annu. Rev. Earth Planet. Sci.* **28**, 611–667 (2000).
2. Kasting, J. F. The Goldilocks planet? How silicate weathering maintains Earth 'just right'. *Elements* **15**, 235–240 (2019).
3. Penman, D. E., Caves Rugenstein, J. K., Ibarra, D. E. & Winnick, M. J. Silicate weathering as a feedback and forcing in Earth's climate and carbon cycle. *Earth Sci. Rev.* **209**, 103298 (2020).
4. Raymo, M. E. & Ruddiman, W. F. Tectonic forcing of late Cenozoic climate. *Nature* **359**, 117–122 (1992).
5. Berner, R. A. & Berner E. K. in *Tectonic Uplift and Climate Change* (ed. Ruddiman, W. F.) 353–365 (Springer, 1997).
6. Walker, J. C. G., Hays, P. B. & Kasting, J. F. A negative feedback mechanism for the long-term stabilization of Earth's surface temperature. *J. Geophys. Res. Oceans* **86**, 9776–9782 (1981).
7. Edmond, J. M. Himalayan tectonics, weathering processes, and the strontium isotope record in marine limestones. *Science* **258**, 1594–1597 (1992).
8. McKenzie, N. R. et al. Continental arc volcanism as the principal driver of icehouse–greenhouse variability. *Science* **352**, 444–447 (2016).
9. Macdonald, F. A., Swanson-Hysell, N. L., Park, Y., Lisiecki, L. & Jagoutz, O. Arc–continent collisions in the tropics set Earth's climate state. *Science* **364**, 181–184 (2019).
10. Hincks, T., Aspinall, W., Cooke, R. & Gernon, T. Oklahoma's induced seismicity strongly linked to wastewater injection depth. *Science* **359**, 1251–1255 (2018).
11. Matthews, K. J. et al. Global plate boundary evolution and kinematics since the late Paleozoic. *Glob. Planet. Change* **146**, 226–250 (2016).
12. Foster, G. L., Royer, D. L. & Lunt, D. J. Future climate forcing potentially without precedent in the last 420 million years. *Nat. Commun.* **8**, 14845 (2017).
13. Morris, J. L. et al. The timescale of early land plant evolution. *Proc. Natl Acad. Sci. USA* **115**, E2274 (2018).
14. Müller, R. D. et al. GPlates: building a virtual Earth through deep time. *Geochem. Geophys. Geosyst.* **19**, 2243–2261 (2018).
15. Cao, W., Lee, C.-T. A. & Lackey, J. S. Episodic nature of continental arc activity since 750 Ma: a global compilation. *Earth Planet. Sci. Lett.* **461**, 85–95 (2017).
16. Johansson, L., Zahirovic, S. & Müller, R. D. The interplay between the eruption and weathering of large igneous provinces and the deep-time carbon cycle. *Geophys. Res. Lett.* **45**, 5380–5389 (2018).
17. Veizer, J. et al. $^{87}Sr/^{86}Sr$, $\delta^{13}C$ and $\delta^{18}O$ evolution of Phanerozoic seawater. *Chem. Geol.* **161**, 59–88 (1999).
18. Peucker-Ehrenbrink, B. & Fiske, G. J. A continental perspective of the seawater $^{87}Sr/^{86}Sr$ record: a review. *Chem. Geol.* **510**, 140–165 (2019).
19. Elderfield, H. & Schultz, A. Mid-ocean ridge hydrothermal fluxes and the chemical composition of the ocean. *Annu. Rev. Earth Planet. Sci.* **24**, 191–224 (1996).
20. Bataille, C. P., Willis, A., Yang, X. & Liu, X.-M. Continental igneous rock composition: a major control of past global chemical weathering. *Sci. Adv.* **3**, e1602183 (2017).
21. Vérard, C., Hochard, C., Baumgartner, P. O., Stampfli, G. M. & Liu, M. Geodynamic evolution of the Earth over the Phanerozoic: plate tectonic activity and palaeoclimatic indicators. *J. Palaeogeogr.* **4**, 167–188 (2015).

22. Jagoutz, O., Macdonald, F. A. & Royden, L. Low-latitude arc–continent collision as a driver for global cooling. *Proc. Natl Acad. Sci. USA* **113**, 4935–4940 (2016).

23. Donnadieu, Y., Goddéris, Y., Ramstein, G., Nédélec, A. & Meert, J. A 'snowball Earth' climate triggered by continental break-up through changes in runoff. *Nature* **428**, 303–306 (2004).

24. Cogné, J.-P. & Humler, E. Global scale patterns of continental fragmentation: Wilson's cycles as a constraint for long-term sea-level changes. *Earth Planet. Sci. Lett.* **273**, 251–259 (2008).

25. Merdith, A. S., Williams, S. E., Brune, S., Collins, A. S. & Müller, R. D. Rift and plate boundary evolution across two supercontinent cycles. *Glob. Planet. Change* **173**, 1–14 (2019).

26. Granot, R. & Dyment, J. The Cretaceous opening of the South Atlantic Ocean. *Earth Planet. Sci. Lett.* **414**, 156–163 (2015).

27. Fan, J.-x. et al. A high-resolution summary of Cambrian to Early Triassic marine invertebrate biodiversity. *Science* **367**, 272–277 (2020).

28. Hartmann, J., Moosdorf, N., Lauerwald, R., Hinderer, M. & West, A. J. Global chemical weathering and associated P-release—the role of lithology, temperature and soil properties. *Chem. Geol.* **363**, 145–163 (2014).

29. McKenzie, N. R. & Jiang, H. Earth's outgassing and climatic transitions: the slow burn towards environmental 'catastrophes'? *Elements* **15**, 325–330 (2019).

30. Hart, S. R., Erlank, A. J. & Kable, E. J. D. Sea floor basalt alteration: some chemical and Sr isotopic effects. *Contrib. Mineral. Petrol.* **44**, 219–230 (1974).

31. Mottl, M. J. & Wheat, C. G. Hydrothermal circulation through mid-ocean ridge flanks: fluxes of heat and magnesium. *Geochim. Cosmochim. Acta* **58**, 2225–2237 (1994).

32. Müller, R. D., Dutkiewicz, A., Seton, M. & Gaina, C. Seawater chemistry driven by supercontinent assembly, breakup, and dispersal. *Geology* **41**, 907–910 (2013).

33. Coggon, R. M., Teagle, D. A. H., Smith-Duque, C. E., Alt, J. C. & Cooper, M. J. Reconstructing past seawater Mg/Ca and Sr/Ca from mid-ocean ridge flank calcium carbonate veins. *Science* **327**, 1114–1117 (2010).

34. Booij, E., Gallahan, W. E. & Staudigel, H. Ion-exchange experiments and Rb/Sr dating on celadonites from the Troodos ophiolite, Cyprus. *Chem. Geol.* **126**, 155–167 (1995).

35. Blum, J. D. & Erel, Y. A silicate weathering mechanism linking increases in marine $^{87}Sr/^{86}Sr$ with global glaciation. *Nature* **373**, 415–418 (1995).

36. Prestrud Anderson, S., Drever, J. I. & Humphrey, N. F. Chemical weathering in glacial environments. *Geology* **25**, 399–402 (1997).

37. Vance, D., Teagle, D. A. H. & Foster, G. L. Variable Quaternary chemical weathering fluxes and imbalances in marine geochemical budgets. *Nature* **458**, 493–496 (2009).

38. Lee, C.-T. A., Thurner, S., Paterson, S. & Cao, W. The rise and fall of continental arcs: interplays between magmatism, uplift, weathering, and climate. *Earth Planet. Sci. Lett.* **425**, 105–119 (2015).

39. Jiang, H. & A. Lee, C.-T. On the role of chemical weathering of continental arcs in long-term climate regulation: a case study of the Peninsular Ranges batholith, California (USA). *Earth Planet. Sci. Lett.* **525**, 115733 (2019).

40. Allègre, C. J. et al. The fundamental role of island arc weathering in the oceanic Sr isotope budget. *Earth Planet. Sci. Lett.* **292**, 51–56 (2010).

41. Park, Y. et al. Emergence of the Southeast Asian islands as a driver for Neogene cooling. *Proc. Natl Acad. Sci. USA* **117**, 25319–25326 (2020).

42. West, A. J., Galy, A. & Bickle, M. Tectonic and climatic controls on silicate weathering. *Earth Planet. Sci. Lett.* **235**, 211–228 (2005).

43. Gaillardet, J., Louvat, P. & Lajeunesse, E. Rivers from volcanic island arcs: the subduction weathering factory. *Appl. Geochem.* **26**, S350–S353 (2011).

44. McClain, M. E. & Naiman, R. J. Andean influences on the biogeochemistry and ecology of the Amazon River. *BioScience* **58**, 325–338 (2008).

45. O'Nions, R. K., Hamilton, P. J. & Evensen, N. M. Variations in $^{143}Nd/^{144}Nd$ and $^{87}Sr/^{86}Sr$ ratios in oceanic basalts. *Earth Planet. Sci. Lett.* **34**, 13–22 (1977).

46. Brady, O. V. & Gíslason, S. R. Seafloor weathering controls on atmospheric CO_2 and global climate. *Geochim. Cosmochim. Acta* **61**, 965–973 (1997).

47. Lee, C.-T. A. & Bachmann, O. How important is the role of crystal fractionation in making intermediate magmas? Insights from Zr and P systematics. *Earth Planet. Sci. Lett.* **393**, 266–274 (2014).

48. Beerling, D. J. et al. Potential for large-scale CO_2 removal via enhanced rock weathering with croplands. *Nature* **583**, 242–248 (2020).

49. Mason, E., Edmonds, M. & Turchyn, A. V. Remobilization of crustal carbon may dominate volcanic arc emissions. *Science* **357**, 290–294 (2017).

50. Witkowski, C. R., Weijers, J. W. H., Blais, B., Schouten, S. & Sinninghe Damsté, J. S. Molecular fossils from phytoplankton reveal secular p_{CO_2} trend over the Phanerozoic. *Sci. Adv.* **4**, eaat4556 (2018).

Methods

BN analysis. Here we outline the methodology for our Bayesian analysis. A BN is a directed acyclic graph. It comprises a set of variables (which can represent discrete or continuous quantities) and a set of directed edges (arcs) between the variables, with the condition that the edges do not form a directed cycle. This means there are no loops (a node cannot be connected to itself) and no cycles (no path that leads from a node, via other nodes, back to itself). There is no requirement for the links to represent causal relationships. We use the UNINET COM library[51] in Visual Studio (C++)[52] to perform data mining on the time series detailed in the 'Network nodes' section (below). UNINET represents the graphical model using the joint normal copula (for example, ref. [10]), allowing fast and efficient modelling of complex multivariate dependencies. The approach enables the identification of dominant correlations for a range of geophysical and geochemical variables with the strontium isotope ratio of seawater (^{87}Sr/^{86}Sr)$_{sw}$ through geological time as a proxy for global chemical weathering[17,20]. All initial data processing and GIS analysis are performed in R[53].

Our analysis considers data for the period from 410 Ma to 0 Ma using regularized time series with a time step of 0.5 Myr. These time series are provided in Supplementary Data 1 (Fig. 1). As many of the individual time series are based on measurements, estimates or model values irregularly spaced in time, we interpolate to obtain regular (0.5 Myr) time series to match the resolution of the CO_2 record used[12]. For cases with multiple observations in a given time interval, a moving average is applied (again with a 0.5 Myr window). The number of original data points before interpolation (and accounting for lags) is used to estimate confidence interval thresholds (CI$_{thresh}$) for rank correlation coefficients for each of the variables with (^{87}Sr/^{86}Sr)$_{sw}$. The CI (in this case the 99th percentile) threshold determines whether a particular lagged variable is retained in the model (described in the 'Summary of the data-mining algorithm' section). To investigate the potential time lags between the various processes and Sr, we calculate average values for each of the predictor variables with lead times up to 50 My in 2.5 Myr intervals. A correlation at zero lag means the processes occur within the same time step (t, Myr). A lag of 2.5 corresponds to the correlation between Sr and the average value for a variable in the interval ($t - 2.5$) to ($t - 0.5$) Myr and so on as we are interested in how Sr lags the various geological processes. The one exception to this is Extended Data Fig. 1, where we present correlations for Sr leading CO_2.

We also repeated the BN data mining using 1-Myr-interval input data, and the differences in the results were negligible. We impose CI thresholds on the basis of the original number of observations, not the length of the interpolated time series.

Uncertainty analysis. To investigate the effect of uncertainty in the original input data, we simulated 1,000 variant time series for each parameter and used this alternative dataset to test the BN analysis and search algorithm. For each input parameter (with the exception of p_{CO_2}, where variant time series outputs from Foster et al.[12] were used directly), we performed random sampling to generate multiple alternative time series at the same resolution as the original data. Each simulated input time series was then interpolated to produce a regular 0.5 Myr time series, and time lags were calculated in the same manner as for the original input dataset.

In some cases, there are existing models of variability (for example, for p_{CO_2})[12] or published error estimates (for example, upper and lower bounds for continental arc length[15]), and we can directly apply these 'known' uncertainties. For other parameters, we have to make reasonable assumptions on the basis of existing knowledge of the individual processes or model limitations to characterize their uncertainty.

The (^{87}Sr/^{86}Sr)$_{sw}$ and igneous Sr ratio were treated slightly differently from the inputs derived from tectonic reconstructions or proxy records because these curves are well established and based on several thousand individual direct measurements across the period of interest. Therefore, it is reasonable to accept that the variability present in the raw data (for example, Fig. 1g) provides a good approximation of the 'true' uncertainty. Rather than simulating additional noise, we vary the width of the time window used to calculate a moving average.

Fundamentally, characterizing the uncertainties in many of these processes (for example, global tectonics) is complex because the time series are of differing resolution, and the individual geological processes vary on different timescales. Some processes vary rapidly (on timescales of the order ~1 Myr or less) whereas others (for example, subduction length) are expected to vary more slowly. In addition, there are physical grounds for autocorrelation and correlation between processes, which cannot be explicitly simulated without making many assumptions. To avoid making unjustifiable or overly complex model choices, we use independent random sampling to make perturbations to the original data and thus simulate uncertainty. This is a cautious approach and will reduce correlation (and autocorrelation) for any given variable.

For parameters with no well-defined or widely accepted error bounds, we have attempted to strike a balance between estimating a reasonable level of uncertainty and preserving the physical characteristics of the individual time series (the expected frequency of oscillation in time; for example, arc length is relatively steady over 1–2 Myr, whereas atmospheric CO_2 can vary more rapidly). For several parameters (see the 'Uncertainty distributions' section), we applied increased uncertainty for ages older than ~200 Ma because little oceanic lithosphere of this

age is preserved today[54], leading to greater uncertainty in tectonic simulations that cover the studied period from 410 to 200 Ma. As the BN is learned purely from the data and requires no previous assumptions about conditional dependence between nodes, it can readily be updated should new observations (or better-constrained uncertainty estimates) become available. Thus, our hypotheses are explicitly open to further scrutiny and testing using the same modelling approach.

In our primary analysis, we use a single time series for each parameter that represents the best available evidence. These inputs are all from published time series of observations, model simulations or proxy data. In the following, we detail the process of simulating input uncertainty for each parameter in turn. These simulated time series (and associated time lags) were combined into a single input data file (~3 GB size, comprising 1,000 individual variant time series for 253 nodes, including lags) and used to test the BN by:

1. Calculating the empirical and BN correlations for all variables/lags and comparing the results with calculations for the original 'best estimate' input data (Extended Data Fig. 4)
2. Running the BN node search algorithm to identify the variables/lags that provide the most information about (^{87}Sr/^{86}Sr)$_{sw}$ and again comparing these results with the search using the original input data

Network nodes and uncertainty distributions. The principal aim of our analysis is to identify the variables that are most strongly correlated with (^{87}Sr/^{86}Sr)$_{sw}$ (the 'node of interest'), and at what time lags, to quantitatively understand the primary geological processes driving chemical weathering. We used the variation in (^{87}Sr/^{86}Sr)$_{sw}$ ratios derived from marine carbonates[17] (Fig. 1g).

These raw (^{87}Sr/^{86}Sr)$_{sw}$ data produce an irregular time series with around 5,900 individual data points spanning the interval from 410 to 0 Ma, with a maximum interval of 10.2 Myr. To generate a regular time series for our node of interest, we took a moving average of (^{87}Sr/^{86}Sr)$_{sw}$ using a rolling window of ±0.25 Myr. We do not consider lagged values for Sr here as we are interested primarily in identifying the processes that lead (^{87}Sr/^{86}Sr)$_{sw}$. We do, however, present a separate analysis of the relationship between lagged (^{87}Sr/^{86}Sr)$_{sw}$ and CO_2 (Extended Data Fig. 1).

Network nodes. The following variables are investigated.

Plate-tectonic fragmentation. Continental areas were estimated from shapefiles generated by the open-source plate-tectonic reconstruction software GPlates[14,55]. We used the plate-tectonic reconstruction of Matthews et al.[11] for extracting latitudinal and time-sensitive data for our analysis. This plate model is a synthesis of the Domeier and Torsvik[67] model for the Late Palaeozoic and the Müller et al.[56] model for the Mesozoic and Cenozoic. All data were extracted with the plate model in a palaeomagnetic reference frame, and the output comprises georeferenced maps of continent boundaries at 1 Myr intervals from 410 Ma to the present. Areas were calculated by taking continental polygons (which characterize the shapes and locations of all the continental land masses) from the GPlates shapefiles[11] and splitting them into six bands according to latitude (90–20° N, 20–10° N, 10–0° N, 0–10° S, 10–20° S, 20–90° S). The Rsaga package function rsaga.intersect.polygons is used to split the continental shapes by latitude, working in the World Geodetic System 84 global reference system coordinates (EPSG:4326). The total continental area within each latitude band is calculated by first 'dissolving' and cleaning the polygons using the rsaga.geoprocessor function shapes–polygons then calculating the total area using the areaPolygon function from the Rgeosphere package. Area is calculated in m^2 and—accounting for the accuracy of shapefiles and the coordinate transformation from longitude/latitude—is considered accurate to approximately two significant figures. This is reasonable given the model uncertainty and resolution. We measured the perimeter of continental land masses through time using the perimeter function from the Rgeosphere package and adapted the method of Cogné and Humler[24] and Merdith et al.[25] to compute the continental perimeter/area ratio—a measure of how 'fragmented' the continents are through time (Fig. 1f and Supplementary Data 1). In contrast to ref. [25], we do not apply a minimum area threshold as, for the period we are considering, we require only the reconstructions of Matthews et al.[11] and do not need to incorporate other plate models of variable spatial resolution. We do, however, remove 'holes' with areas $<5 \times 10^{11}$ m^2 to eliminate the extremely narrow void spaces (slithers) that occur where adjacent continental polygons never fully join due to their geometry and resolution in the model. Leaving these 'holes' in place inflates the perimeter estimate at certain time steps, and they can be clearly identified as erroneous gaps from inspection of the individual shapefiles. Units of fragmentation are m^{-1} (perimeter/area) and are extracted at 1.0 Myr intervals then interpolated to 0.5 Myr.

Land surface area within the tropics. The area of the continental land surface (a) within 10° of the Equator (the tropical rain belt[9]) and (b) ±20° of the Equator were measured as described in the preceding account, again using shapefiles exported from GPlates and processed in R. The latitudinal distribution of continental land masses (within both ±20° (Fig. 1f) and ±10° bands) and the fractional areas of continental land masses in the equatorial bands (area within the belt divided by the total crustal area) through time are shown in Extended Data Figure 7, and the data are available in Supplementary Data 1. The result is a 1-Myr-interval time series (units: m^2), interpolated to 0.5 Myr for the BN analysis.

Seafloor production rates. We calculated seafloor production rates as the product of ridge length and spreading rate of each discrete spreading segment (each mid-ocean-ridge segment separated by a transform boundary) at 1 Myr time steps using the pyGPlates python library[57]. The data were extracted from the Matthews et al.[11] plate model. The spreading segments were defined by obtaining the tangent to the midpoint of the spreading segment and measuring the angle between this and the great circle of the stage-pole orientation (spreading direction) that passes through the segment midpoint (Extended Data Fig. 8). If this angle exceeds 70°, it is assumed to represent a spreading segment, and the full spreading rate was extracted and multiplied by the length of the segment. The sum of all segments × full spreading rate was calculated at 1 Myr intervals to give total seafloor production. Further details on this approach are provided in Extended Data Fig. 8. A key uncertainty in the construction of seafloor production rates is that very little oceanic lithosphere older than 200 Ma is preserved today[54]. However, our analysis does not concern time-sensitive evolution of oceanic lithosphere (such that is required for understanding how oceanic volume changes through time or the delivery of volatiles to trenches, for example). Instead, we require just a measure of the volume of new crust formed through time. The global tectonic models used to estimate our seafloor production rates are underpinned by many geological constraints. For example, Atlantic-style oceans that opened during the Palaeozoic (for example, the Mesotethys and Neotethys oceans) are well constrained by rift–drift records and palaeomagnetic data, allowing a first-order estimate of ocean basin evolution as implemented in plate models. The Panthalassa Ocean basin in the Matthews et al.[11] model was constructed by Domeier and Torsvik[67] to ensure that spreading rate and ridge length were sufficient to ensure convergence at all subduction zones that encircled the ocean basin. We therefore consider that—while a non-unique solution—the evolution of this ocean basin in the Palaeozoic provides a robust minimum estimate of the volume of ocean crust added to the globe over this time. Finally, one of the implications of our analysis for the past 410 Myr is that seafloor production rate exerts a relatively weak control on $(^{87}Sr/^{86}Sr)_{sw}$ through time. To test the sensitivity of this result to the uncertainty in spreading rates before 200 Ma, we developed a BN for the past 200 Myr, when seafloor spreading rates are much better constrained. We found that the empirical correlation between seafloor production rates and $(^{87}Sr/^{86}Sr)_{sw}$ reduces even further (relative to the 410 Myr network; from −0.28 to −0.16). This test, targeting the interval with the highest certainty, provides confidence that seafloor production rate is of secondary importance in global chemical weathering and has been particularly weak since the early Jurassic. The output is a 1-Myr-interval time series (units: $km^2 Myr^{-1}$), which we interpolate to 0.5 Myr for the purpose of our analysis.

Continental arc length. We used a global compilation of continental volcanic arc lengths[15] that is based on the spatial extent of granitoids, currently exposed at the Earth's surface, associated with continental arc magmatism. Accordingly, these estimates are independent from any plate model used in our analysis. Here, the minimum length is based on the actual (observed) extent of the surface exposure of the granitoids, and the maximum length is based on the geological interpretation of the original spatial extent of the arcs (described in the supplementary information accompanying Cao et al.[15]). It must be noted that, for the present day, these estimates omit several areas experiencing continental subduction (for example, under Zealandia, flat slab subduction in the Andes). In most cases, the minimum and maximum lengths are equal, and in cases where these deviated, we used the average length value—noting that the difference between the minimum/maximum and the average length is <11.5% during the period of interest (Fig. 1c). The time series (units: km) is regular with a 1 Myr interval, interpolated to 0.5 Myr.

Suture-zone length. We used a database of suture-zone length that records sites of ophiolite obduction during arc–continent collisions[9]. Here, the suture-zone lengths were estimated using the observed spatial extent of ophiolites based on published geological maps and global lithological compilations. Macdonald et al.[9] reconstructed the locations of suture zones throughout the Phanerozoic using palaeogeographic models. They estimated the duration of suture-zone activity using the onset of ophiolite obduction (as evidenced by the first occurrence of arc exhumation), which they defined as the first appearance of ophiolite-derived detritus in the foreland, and the termination of foreland deposition was taken to mark the cessation of ophiolite obduction (procedure is described in the supplementary information accompanying ref. [9]). Since the suture 'length' in a region is maintained as long as associated sedimentary deposits are accumulating in the foreland basin[9], the 'duration' measure of Macdonald et al.[9] is considered a crude proxy for the volume of exhumed ophiolites. The time series (units: km) is regular with a 5 Myr interval, interpolated to 0.5 Myr.

Atmospheric CO_2 concentration. We used a compilation of p_{CO_2} for the past 420 Myr derived from multi-proxy measurements ($N = 1,241$; from the literature and covering five independent techniques; ref. [12]). Foster et al.[12] used a set of criteria to screen and standardize these records and applied Monte Carlo resampling and a local polynomial regression (LOESS) fit to the resulting data series. We used the maximum probability p_{CO_2} data from ref. [12] (Supplementary Data 1), with associated 68th and 95th percentile ranges (Fig. 1b). We note that recent phytane-based measurements[50] are in good agreement with this long-term p_{CO_2}

record (Fig. 1b). The time series from Foster et al.[12] (units: ppm) is regular with a 0.5 Myr interval.

Latitudinal ice extent. We used a recent compilation of the latitudinal extent of continental-ice sheets (for example, 90° = no ice sheets) from Macdonald et al.[9]. This compilation is based on a literature review of the geological constraints on glaciation during the Phanerozoic and the inferred palaeogeographic extent of continental ice using updated age constraints (a full discussion of this database is described in the supplementary information accompanying ref. [9]). The time series (units: degrees) is regular with a 1 Myr interval interpolated to 0.5 Myr.

Subduction-zone length. The total length of subduction zones (including oceanic arcs) through geological time were taken from Matthews et al.[11] and extracted using pyGPlates[57] at 1 Myr intervals. Spatial and temporal constraints on the distribution and extent of subduction zones are provided by geological constraints such as ophiolites, subduction-related magmatism and the occurrence of high-pressure metamorphic lithologies that are consistent with subduction processes[58]. As noted by Merdith et al.[58], there are some similarities in the trends of subduction-zone and continental arc lengths[15], lending support to these independently derived measures. The time series is regular at 1 Myr intervals (units: km), interpolated to 0.5 Myr.

Active LIP area. We used the area of LIPs actively erupting at a particular 1 Myr time step from the compilation of Johansson et al.[16]. This database, which includes continental and oceanic LIPs, was compiled and digitized from the literature, and their locations were reconstructed using GPlates software[16]. An underlying assumption of this time series is that the LIPs were active for a total period of 3 Myr after their accepted eruption age. The time series is regular at 1 Myr intervals (units: km^2), interpolated to 0.5 Myr.

Weatherable LIP area in the tropics. We also use the area of LIPs (active or inactive) exposed within 15° of the Equator at a particular 1 Myr time step[16]. Johansson et al.[16] applied palaeogeographic reconstructions to discriminate between continental and oceanic LIPs to isolate exposed (continental) LIPs within the tropics. This regular time series (1 Myr interval, units: km^2) provides a minimum estimate of LIP area through time.

Igneous Sr ratio. We use the $^{87}Sr/^{86}Sr$ ratio of zircon-bearing igneous rocks (i-zig) over the past 400 Myr, from the compilation of Bataille et al.[20] that spans 1,000 Myr, to assess the relative contribution of continental igneous rock lithologies (dominantly continental volcanic arcs, the locus of zircon formation) to $(^{87}Sr/^{86}Sr)_{sw}$. The authors applied a bootstrap resampling approach to correct for geographic/sampling biases in the detrital zircon record comprising 24,715 individual zircon grains. Bataille et al.[20] used the relationship between the ϵHf compositions of zircons and the ϵSr of their igneous host rocks to estimate the secular variations in the $(^{87}Sr/^{86}Sr)_{i-zig}$ through time—reflecting the changing proportion of juvenile and reworked materials generated during orogenesis. We reran code from Bataille et al.[20] using a modified smoothing window of 5 Myr and increment and scale of 0.5 Myr (previously 10 Myr and 1 Myr, respectively, in Bataille et al.[20]). In addition, we applied an adaptive window (decreasing in size) for data points between 5 and 0 Ma to enable extension of the time series to 0.5 Ma.

Uncertainty distributions. For the original input time series for the node of interest, $(^{87}Sr/^{86}Sr)_{sw}$, we used a centred moving average with a window of 0.5 Myr (at each time step, t, we calculated the mean within the window $(t − 0.25)$ to $(t + 0.25)$ Myr). For the uncertainty analysis, the window for the moving average was varied from 1 to 5 Myr by randomly sampling from a uniform distribution on the interval [1,5].

We simulated input uncertainty for each of the predictor nodes as described in the following account, before finally interpolating to give a regular 0.5 Myr time step and calculating time lags up to 50 Myr. We generated 1,000 variant time series for each variable (and associated lags) and merged these into a single input file to perform BN learning. The simulated uncertainties for each node are shown in Extended Data Fig. 2.

Plate-tectonic fragmentation. We consider the rift record of the past 400 Myr to be robust because this interval encompasses only one supercontinent breakup (there is little overprint, and many passive margins have not been inverted)[59]. Here, because little oceanic lithosphere older than 200 Ma is preserved today[54], affecting the fidelity of plate models for this age, we applied increased uncertainty for ages before 200 Ma. For 410–200 Ma, we applied a uniform random variation of up to ±10% and a centred moving average with a 10–15 Myr window (discrete uniform sample). For 200–0 Ma, where the data confidence is greater, we applied a uniform random variation of up to ±5% and a centred moving average with a 5–10 Myr window (discrete uniform sample).

Land surface area within the tropics (a: ±10° of the Equator; b: ±20° of the Equator). Latitude is constrained by palaeomagnetic data, the mean uncertainty of which is approximately 10%[60]. For 410–200 Ma, we applied a conservative ±20% random

variation (uniform distribution) and a centred moving average with a 10–15 Myr window (discrete uniform sample). For 200–0 Ma, we applied a ±10% random variation (uniform distribution) and a centred moving average with a 10–15 Myr window (discrete uniform sample).

Seafloor production rates. Again, seafloor production rates are uncertain because little or no in situ oceanic crust older than ~200 Ma is preserved[54]. To account for this, at each time step from 410–200 Ma, we applied a random variation up to ±10%, sampled from a uniform distribution, which was considered an acceptable range on the basis of existing models of ocean basins[54]. We then took a centred moving average with a variable 2–5 Myr window (sampled from a discrete uniform distribution). For seafloor younger than 200 Ma, we applied ±5% random variation (again using a uniform distribution) and a centred moving average with a 1–2 Myr window (discrete uniform sample). This range is in line with known errors for other parameters in the simulation and reflects the increased uncertainty further back in time.

Continental arc length. Much of the data include estimates for the minimum, maximum and mean continental arc lengths[15]. For cases where only a single estimate is provided (no range was specified in the published compilation), we apply an uncertainty of ±10% of the published values as a reasonable approximation to the upper and lower bounds and assume that the cited value is the mean estimate. This is a cautious but reasonable approach given that, where reported, measured uncertainty is typically of the order ±10% (ref. [15]). Simulated time series were generated by sampling (at each 1 Myr time step) from a beta distribution with the specified minimum, maximum and mean and (in the absence of any more information about the true uncertainty distribution) assuming a standard deviation of 20% of the range. The beta distribution was chosen because it varies smoothly over a fixed interval, and appropriate shape parameters can be readily estimated given the mean, range and standard deviation.

Suture-zone length. The published dataset[9] does not include an estimate of uncertainty. However, the suture-zone records are underpinned by plate simulations that become increasingly uncertain further back in time than 200 Ma. Accordingly, at each 5 Myr time step, in the absence of uncertainty estimates, we varied the data by a randomly sampled (uniform) ±10% for ages older than 200 Ma and ±5% for 200–0 Ma. Again, this range is in line with known errors for other parameters in the simulation (for example, continental arc length), reflects increased uncertainty further back in time and considers the resolution of the original data.

Atmospheric CO_2 concentration. We used 1,000 individual realizations of the multi-proxy CO_2 time series of Foster et al.[12], in which each data point was randomly varied within its age and CO_2 uncertainty. Our original time series for CO_2 uses p_{CO_2} prob max from Foster et al.[12]; this is the modal value from their simulations at each 0.5 Myr time step.

Latitudinal ice extent. The temporal resolution of this dataset is ~1 Myr, although the spatial resolution is fairly coarse because latitude is estimated to the nearest 5°. We therefore chose to vary the values of both time and latitude at each step change, rather than every 1 Myr. This preserves the coarseness of the input rather than introducing artificial 'fast' (short timescale) variability, which is not present in the original data. We applied the following steps:

1. Perturbed the time stamp (for times older than 10 Ma, where there is less certainty about timing of glaciation, we varied the time of each step change by a random amount up to ±0.5 Myr, sampled from a uniform distribution)
2. Perturbed the latitude estimate by a random amount, sampling from a uniform distribution ±2.5°
3. Interpolated to 0.5 Myr and calculated time lags

Subduction-zone length. Subduction-zone length is derived from plate-tectonic reconstructions and is related to both continental arc length and the spatial extent of arc–continental collisions (as indicated by suture-zone length). We therefore followed a similar approach to that used for suture-zone length and continental arc length. For 410–20 Ma, we applied a (uniform) random variation to the length of up to ±10%. Because this is not a rapidly varying process (considerable changes are expected to occur on timescales >1 Myr), we then applied a centred moving average with a 5–10 Myr window (discrete uniform sample). For 200–0 Ma, where length estimates are better constrained, we applied uniform ±5% random variation and a centred moving average with a 5–10 Myr window (discrete uniform sample), again because subduction-zone length is not expected to vary rapidly.

Active LIP area. For 410–200 Ma, we applied a uniform random variation of up to ±20% (again due to the greater uncertainty in model estimates before 200 Ma) and a centred moving average with a 5–10 Myr window (discrete uniform sample). For 200–0 Ma, we applied a uniform random variation of up to ±10% and a centred moving average with a 1–5 Myr window (discrete uniform sample).

Weatherable LIP area in the tropics. This is the same as Active LIP area.

Igneous Sr ratio. This time series was derived from 3,500 individual measurements spanning 410–0 Ma. Here we adopted the method of calculation of Bataille et al.[20] but varied the window used to smooth the data from 2.5 to 7.5 Myr, sampling the window size from a uniform distribution (previously, we used a fixed window of 5 Myr). In addition, the increment (the time step used in the calculations) was varied by randomly sampling from a uniform distribution from 0.25 to 1.25 Myr (previously, we used a fixed increment of 0.5 Myr).

Auto- and cross-correlations. Many of the studied variables are strongly autocorrelated and cross-correlated (for example, due to being different proxies for the same or related processes/states). This makes it very difficult to identify dominant driving processes and their time lags. It is straightforward to compute partial autocorrelations for individual parameters—a standard approach in time-series analysis; however, the multivariate case cannot always be solved. We tested whether the multivariate partial autocorrelation could be computed for our dataset using an R implementation of the PACF[61] (function acf/pacf in the stats package). This function computes the partial lag autocorrelation matrix P(s) of Heyse and Wei[61] (p. 411–414 in Wei[62]), where P(s) is the autocorrelation matrix between Z_t and Z_{t+s} after removing the linear dependency on the vectors at intervening lags Z_{t+1}, Z_{t+2}... Z_{t+s-1}. The elements are normalized correlation coefficients. On the basis of this analysis, we concluded that the multivariate PACF[61] could not successfully be computed for our data.

To provide an alternative means of accounting for the combined effect of multiple parameters (at varying lags) on the variable of interest ($^{87}Sr/^{86}Sr)_{sw}$, we developed a new method based on conditional correlation, estimated using UNINET[51]. The approach we employ is similar in principle to the multivariate partial autocorrelation but evaluates the conditional correlation for variables added iteratively to the BN at increasing time lags.

Code is written in C++ and uses the UNINET Windows COM library[51]. UNINET[51] is a software package for uncertainty analysis and dependence modelling for high dimensional distributions[63,64]. It is available as a standalone application and as a Windows COM library (the UNINET Engine) enabling alternative programming interfaces, including but not limited to R, Matlab and Visual Studio/C++ (used here). UNINET models empirical multivariate distributions by building a joint density function from a set of inputs (data mining). Joint dependency is represented by conditional rank correlation using the joint normal copula[65].

Summary of the data-mining algorithm. Input data are time series for the variable of interest X_t (which, in this instance, is ($^{87}Sr/^{86}Sr)_{sw}$) and the 12 predictor variables A_t, B_t, C_t, ... L_t (variables listed in the 'Network nodes' above), plus lagged values of those variables $A_{t-2.5}$... A_{t-50} and so on. Nodes are grouped and evaluated in order of increasing lag, giving a set of observables (A_t, B_t, C_t, ... L_t) at lag zero; ($A_{t-2.5}$, $B_{t-2.5}$, ... $L_{t-2.5}$) at lag $t - 0.5$ Myr to $t - 2.5$ Myr and so on up to 50 Myr.

We construct the network by starting with the unlagged variable with the highest empirical correlation with ($^{87}Sr/^{86}Sr)_{sw}$, then systematically search through the set of remaining predictor variables to find maximum values of conditional correlation (C_{Cond}) at increasing time lags. At each iteration, we look for the largest C_{Cond} as this identifies the variable that individually provides the maximum additional information at each step. The variable with the largest C_{Cond} is subsequently added to the network if all of the following conditions are met:

1. Its conditional correlation C_{Cond} (the correlation with ($^{87}Sr/^{86}Sr)_{sw}$, conditional on all other variables in the network) exceeds a specified confidence interval threshold. Here we use the 99% CI, with the threshold depending on the number of observations used to generate the time series for the variable in question. This results in a higher threshold for lower-resolution variables.
2. The difference between the (unconditional) empirical rank correlation C_{Emp} and BN (modelled) rank correlation C_{BN} with ($^{87}Sr/^{86}Sr)_{sw}$ is less than 30%. This eliminates variables that cannot be represented accurately by the BN (using normal copulae) and prevents such nodes affecting the estimates of conditional dependence for subsequent nodes.
3. The variable is not highly correlated (a correlation of 0.8 or greater) with any existing variables in the network (nodes higher up in the network hierarchy). This reduces the effect of collinearity.

This procedure is repeated for each discrete time lag, resulting in the lagged variables being either added to the network (in order of decreasing conditional correlation and increasing lag, respectively) or rejected for not meeting one of the preceding three criteria. These steps ensure the construction of a parsimonious model where only the most informative nodes are retained. We present the calculated empirical, BN (modelled) and conditional (modelled) rank correlations for each variable and time lag in Fig. [4] and Extended Data Figs. 3 and 4.

The computational efficiency of UNINET means that this approach is suitable for application to large numbers (of the order hundreds to thousands) of nodes—greater than demonstrated here.

Itemized steps to construct the network.

1. Generate a saturated BN using all variables (nodes) with lag zero (A_t, B_t, C_t... X_t) and identify the node with the largest empirical correlation (C_{Emp}) with the

variable (node) of interest $\mathbf{X}_t$. This node (for example, $\mathbf{C}_t$) individually gives the most information about $\mathbf{X}_t$, so it is placed first in the network hierarchy. The variable of interest $\mathbf{X}_t$ always remains last in the hierarchy as we are interested in computing the probabilty of $\mathbf{X}_t$ given all the other observables. (Note that a saturated BN contains arcs linking every pair of nodes in the network).

2. Step through all the remaining nodes with lag zero ($\mathbf{A}_t,... \mathbf{L}_t$) and add them one by one, as a second 'test node' in the network. Calculate the conditional rank correlation c for each test node in turn, for example, $c = C_{Cond}(\mathbf{X}_t\mathbf{A}_t | \mathbf{C}_t)$. Poor fit (how well the BN can represent dependency with the node of interest) is penalized by calculating $c' = (1-p)c$, where p is a penalty value based on the absolute fractional difference between the empirical and BN correlations ($C_{Emp}(\mathbf{X}_t\mathbf{A}_t)$ and $C_{BN}(\mathbf{X}_t\mathbf{A}_t)$, respectively); that is, if these are the same, the penalty p is zero:

$$p = \text{abs}((C_{Emp}(X_tA_t) - C_{BN}(X_tA_t))/C_{Emp}(X_tA_t))$$

This prioritizes inclusion of nodes that can be represented most accurately by the BN.

3. Find the node that has the largest (absolute) value c' (c'_{max}). If the conditional correlation c is below the specified confidence interval threshold set for this particular node, or if $P > 0.3$ (the BN and empirical correlations differ by more than 30%), the node is eliminated and not added to the network (in this case, move to step 5).

4. Reduce collinearity (high correlations between predictor nodes) as follows. If the node giving c'_{max} has not already been eliminated in step 3, calculate the empirical correlation of this node with all other nodes higher in the BN hierarchy (all nodes other than the node of interest, $\mathbf{X}_t$). If this returns an empirical correlation greater than a given threshold (in this case, 0.8), indicating high collinearity, the node is eliminated and not added to the network. If the empirical correlations are all below 0.8, add the node to the network and proceed to step 5.

5. Repeat steps 2 through 4 with all remaining lag-zero nodes until they are all either added to or eliminated from the network.

6. Repeat steps 2 through 5 using the set of nodes with lag 0.5–2.5 Myr ($\mathbf{A}_{t-2.5}$, $\mathbf{B}_{t-2.5}, ... \mathbf{L}_{t-2.5}$) and so on up to the maximum lag (50 Myr). Using the resulting network, we can then compute and plot the conditional rank correlation for each variable at increasing lag, having effectively removed both the effect of shorter-period lags, and other more-informative predictor variables (Fig. 4 and Extended Data Figs. 3 and 4).

Data availability

All data generated or analysed during this study are provided in the online version of this article (Supplementary Data 1–3) and in Extended Data Tables 1 and 2. These data are also available via FigShare at https://doi.org/10.6084/m9.figshare.14877099 (Supplementary Data 1), https://doi.org/10.6084/m9.figshare.14877132 (Supplementary Data 2) and https://doi.org/10.6084/m9.figshare.14877162 (Supplementary Data 3). Source data are provided with this paper.

Code availability

More details on the computational methods and tools used for this study are available from the corresponding author upon reasonable request.

References

51. Ababei, D. *Uninet* (Lighttwist Software, 2020); https://lighttwist-software.com/uninet/
52. *Develop C and C++ Applications* (Microsoft, 2020); https://visualstudio.microsoft.com/vs/features/cplusplus/
53. The R Project for Statistical Computing (R Foundation, 2020); https://cran.r-project.org/
54. Müller, R. D., Sdrolias, M., Gaina, C. & Roest, W. R. Age, spreading rates, and spreading asymmetry of the world's ocean crust. *Geochem., Geophys. Geosyst.* **9**, Q04006 (2008).
55. GPlates (University of Sydney, 2020); https://www.gplates.org/
56. Müller, R. D. et al. Ocean basin evolution and global-scale plate reorganization events since Pangea breakup. *Annu. Rev. Earth Planet. Sci.* **44**, 107–138 (2016).
57. PyGPlates library for GPlates functionality using the Python programming language (University of Sydney, 2020); https://www.gplates.org/docs/pygplates/
58. Merdith, A. S. et al. A full-plate global reconstruction of the Neoproterozoic. *Gondwana Res.* **50**, 84–134 (2017).
59. Celâl Şengör, A. M., Natalin, B. A., Ernst, R. E. & Buchan, K.L. Rifts of the world. *Geol. Soc. Am. Spec. Pap.* **352**, 389–482 (2001).
60. Torsvik, T. H. et al. Phanerozoic polar wander, palaeogeography and dynamics. *Earth Sci. Rev.* **114**, 325–368 (2012).
61. Heyse, J. F. & Wei, W. W. S. Modelling the advertising–sales relationship through use of multiple time series techniques. *J. Forecast.* **4**, 165–181 (1985).
62. Wei, W. W. S. *Time Series Analysis* (Addison-Wesley, 1990).
63. Ale, B. et al. *Causal Model for Air Transport Safety* Technical Report (NLR Air Transport Safety Institute, 2009).
64. Ale, B. J. M. et al. Further development of a causal model for air transport safety (CATS): building the mathematical heart. *Reliab. Eng. Syst. Saf.* **94**, 1433–1441 (2009).
65. Kurowicka, D. & Cooke, R. *Uncertainty Analysis with High Dimensional Dependence Modelling* (Wiley, 2006).
67. Domeier, M. & Torsvik, T. H. Plate tectonics in the late Paleozoic. *Geosci. Front.* **5**, 303–350 (2014).
66. Stern, C. R. Active Andean volcanism: its geologic and tectonic setting. *Rev. Geol. Chile* **31**, 161–206 (2004).

Author contributions

T.M.G. conceived the idea, led the study, interpreted the data and prepared the manuscript and figures. T.K.H. performed the modelling, designed the network and carried out the analysis, with input from T.M.G. A.S.M. calculated the seafloor production rates, and both A.S.M. and R.D.M. provided support with GPlates and pyGPlates. M.R.P. and C.P.B. provided support with Sr isotope interpretation, and C.P.B. provided normalized Sr data. G.L.F. provided CO_2 data, and both G.L.F. and E.J.R. assisted with palaeoclimate interpretation. T.M.G. wrote the manuscript with input from all co-authors.

Competing interests

The authors declare no competing interests.

Additional information

Extended data is available for this paper at https://doi.org/10.1038/s41561-021-00806-0.

Supplementary information The online version contains supplementary material available at https://doi.org/10.1038/s41561-021-00806-0.

Correspondence and requests for materials should be addressed to T.M.G.

Peer review information *Nature Geoscience* thanks N. Ryan McKenzie, Hehe Jiang and the other, anonymous, reviewer(s) for their contribution to the peer review of this work. Primary Handling Editor: Rebecca Neely, in collaboration with the *Nature Geoscience* team.

**Reprints and permissions information** is available at www.nature.com/reprints.
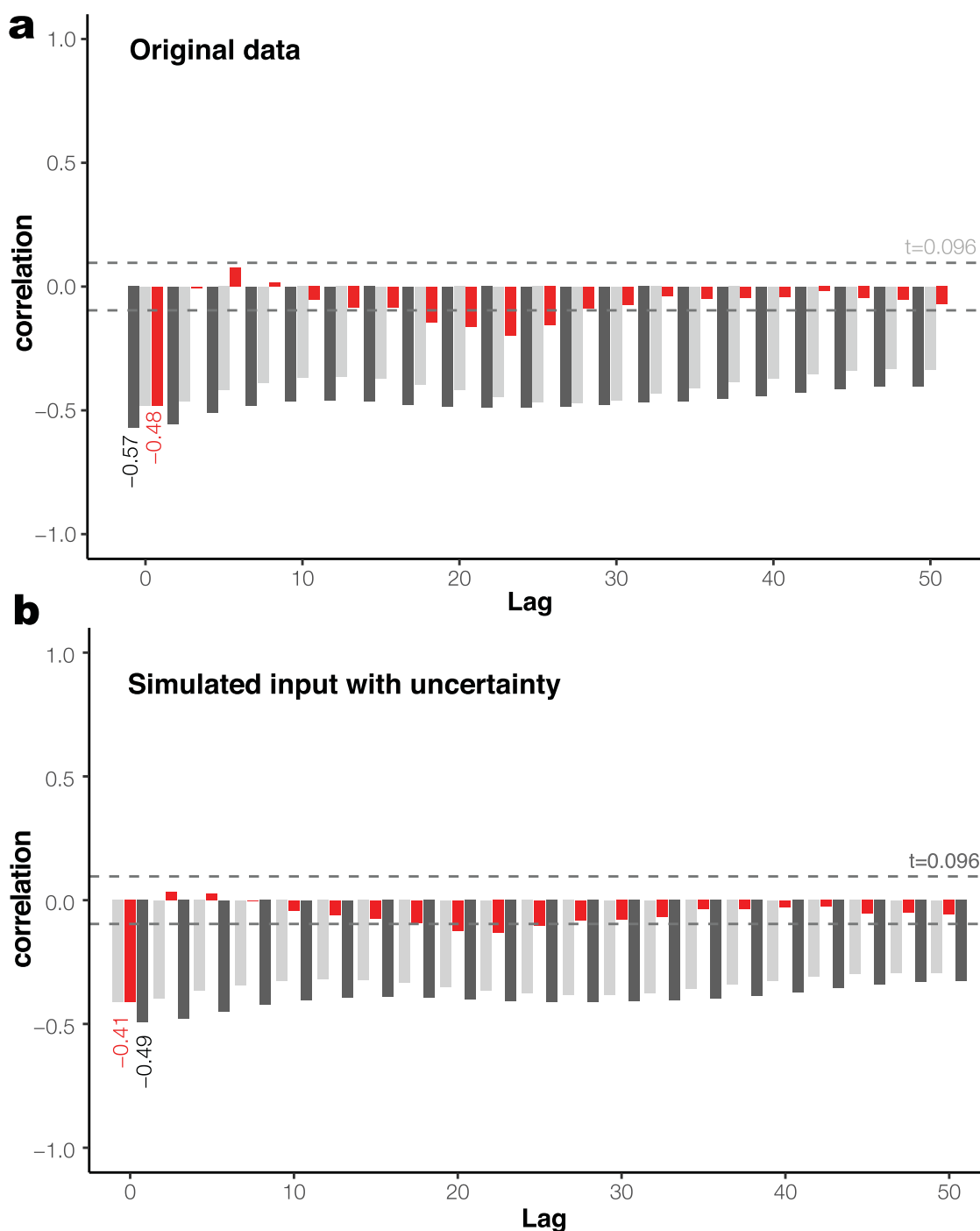
Extended Data Fig. 1 | Relationship between seawater Sr composition and atmospheric CO$_2$ since 410 Ma. Bar plots showing the empirical rank correlation (Spearman's rank correlation, in dark grey), BN rank correlation (modelled, light grey), and BN conditional rank correlation (modelled, red) for pCO$_2$, and (^{87}Sr/^{86}Sr)$_{sw}$, at lags from 0 to 50 Myr (that is, showing where pCO$_2$ lags Sr). We present results for (a) the best estimate input time series (most probable values for pCO$_2$ from Foster et al.[12]), and (b) using a set of 1,000 individual time series that captures the uncertainty in pCO$_2$ and (^{87}Sr/^{86}Sr)$_{sw}$. Here, the conditional rank correlation is the correlation between the two variables at a given lag, accounting for the effects of all shorter lags—similar in principle to the multivariate partial autocorrelation. The horizontal dashed lines denote 99% confidence intervals (t = 0.096). Note that the relationship between (^{87}Sr/^{86}Sr)$_{sw}$ and atmospheric CO$_2$ is strongest at short (that is, zero) time lags (conditional correlation = -0.48), suggesting that the processes controlling seawater Sr influence atmospheric CO$_2$ predominantly on short (<1 Myr) timescales. The conditional rank correlation of seawater Sr and CO$_2$ at a lag of 20-25 Myr (albeit relatively weak) could either be due to some delayed Earth system response, or a correlation between Sr and another process driving CO$_2$ variation on a different timescale. Note the reduction in the strength of the empirical and conditional correlations with the addition of input uncertainty.
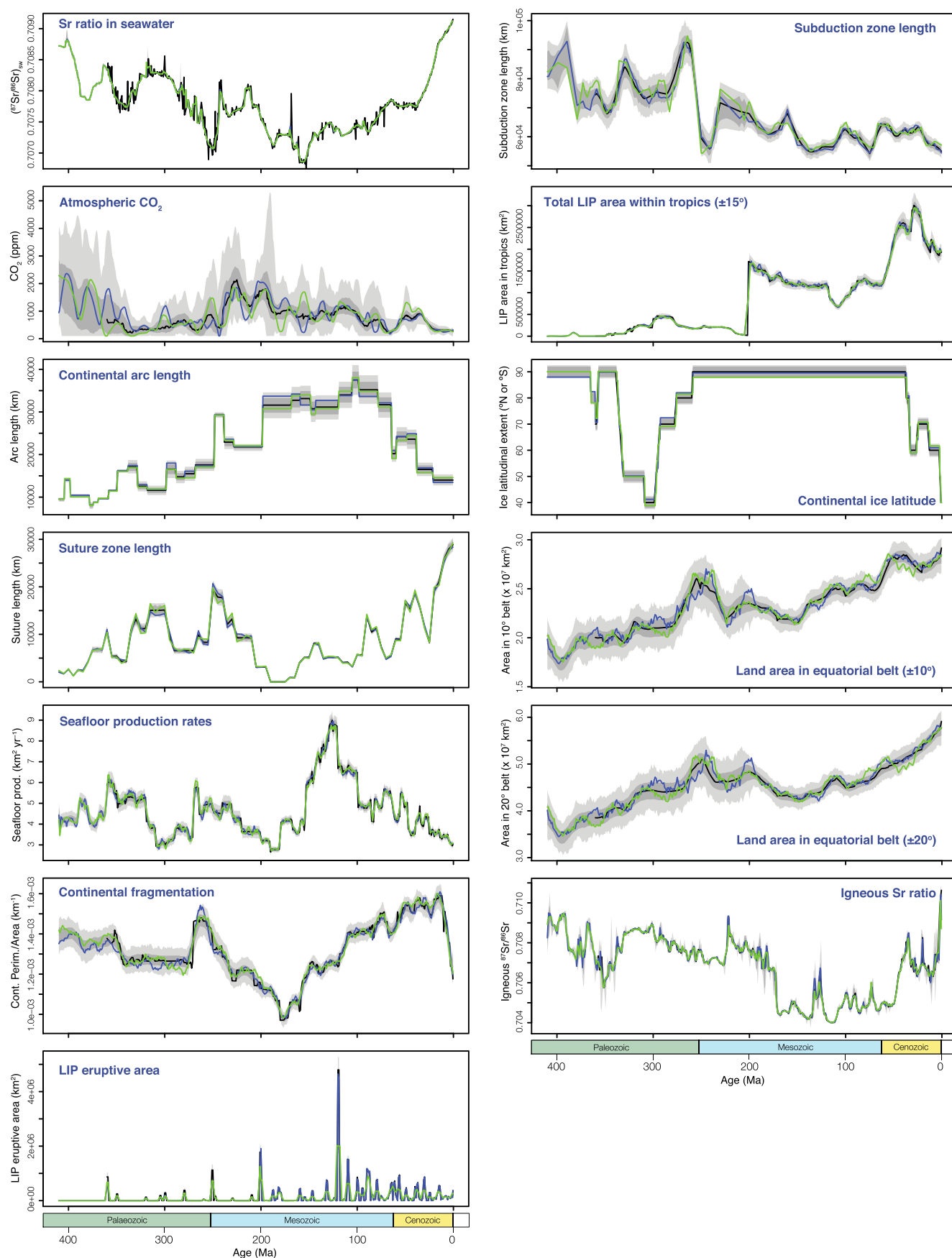
**Extended Data Fig. 2 | See next page for caption.**

Extended Data Fig. 2 | All tectonic, volcanic, geochemical and climate time series used in the network, and their uncertainty estimates. See the Methods for full details of the uncertainties for each variable. The black line denotes the original input time series (mean values or 'best estimates' from both our analysis and prior studies). The shaded envelopes represent minimum and maximum values (light grey) and 90th and 10th percentiles (dark grey). The blue and green lines are examples of single realizations from the simulated input data set; that is, individual time-series that form part of the alternative data set used to investigate the effect of input uncertainty on the strength of correlations with $(^{87}Sr/^{86}Sr)_{sw}$.
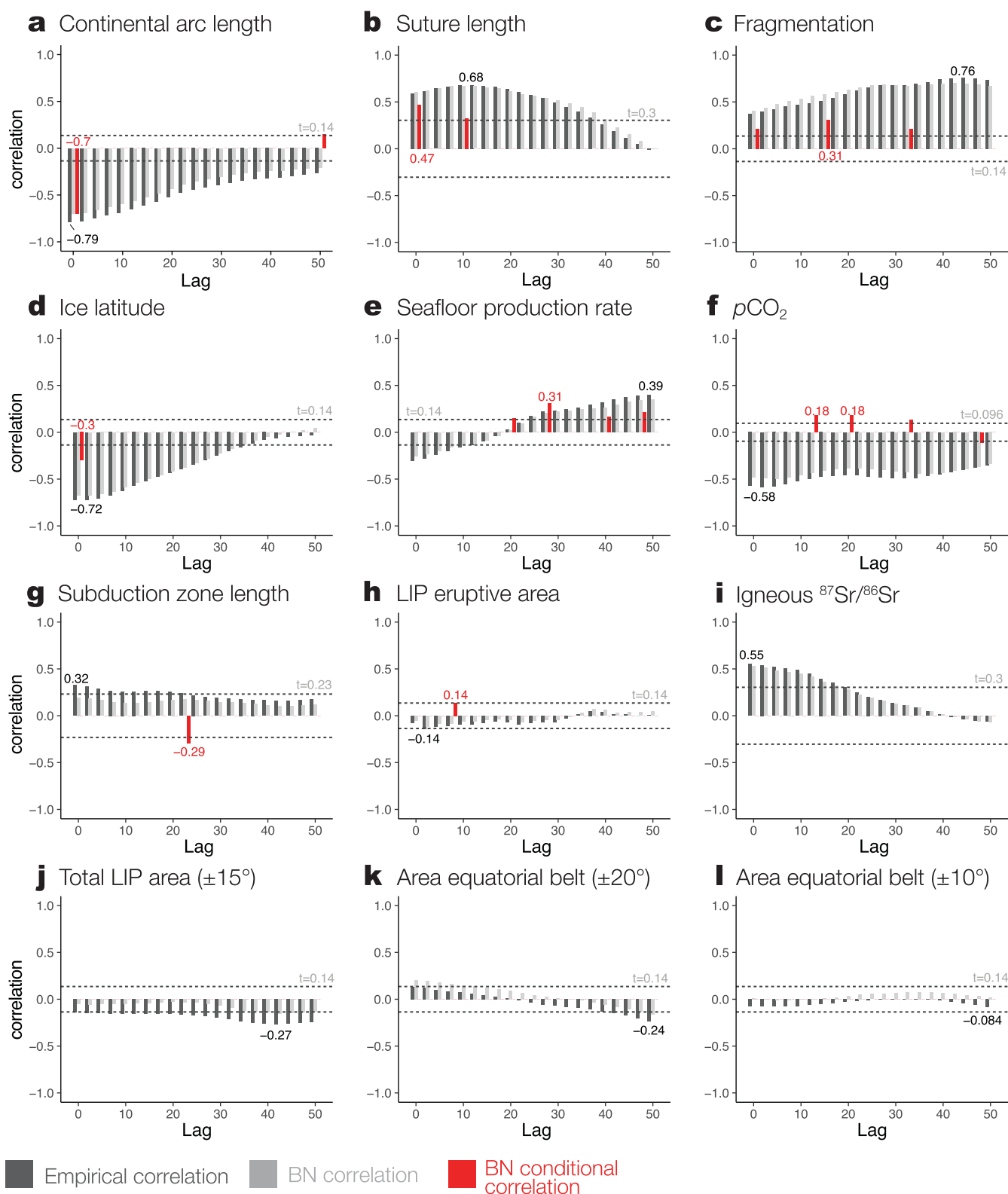
**Extended Data Fig. 3 | The correlations of geologic processes with (^{87}Sr/^{86}Sr)$_{sw}$ and their time lags.** The plots show the empirical rank correlations (C_{Emp}), Bayesian Network correlations (C_{BN}), and BN conditional rank correlations (C_{Cond}), at time lags from 0 to 50 Myr in 2.5 Myr intervals, using the original, best estimate input data (Supplementary Data File S1). The values shown in dark grey on the plots are the highest absolute values of C_{Emp}, and those in red are the highest absolute C_{Cond}. Horizontal dashed lines denote the confidence intervals for each node (t, light grey text), estimated based on the resolution of the original input data (before interpolation).
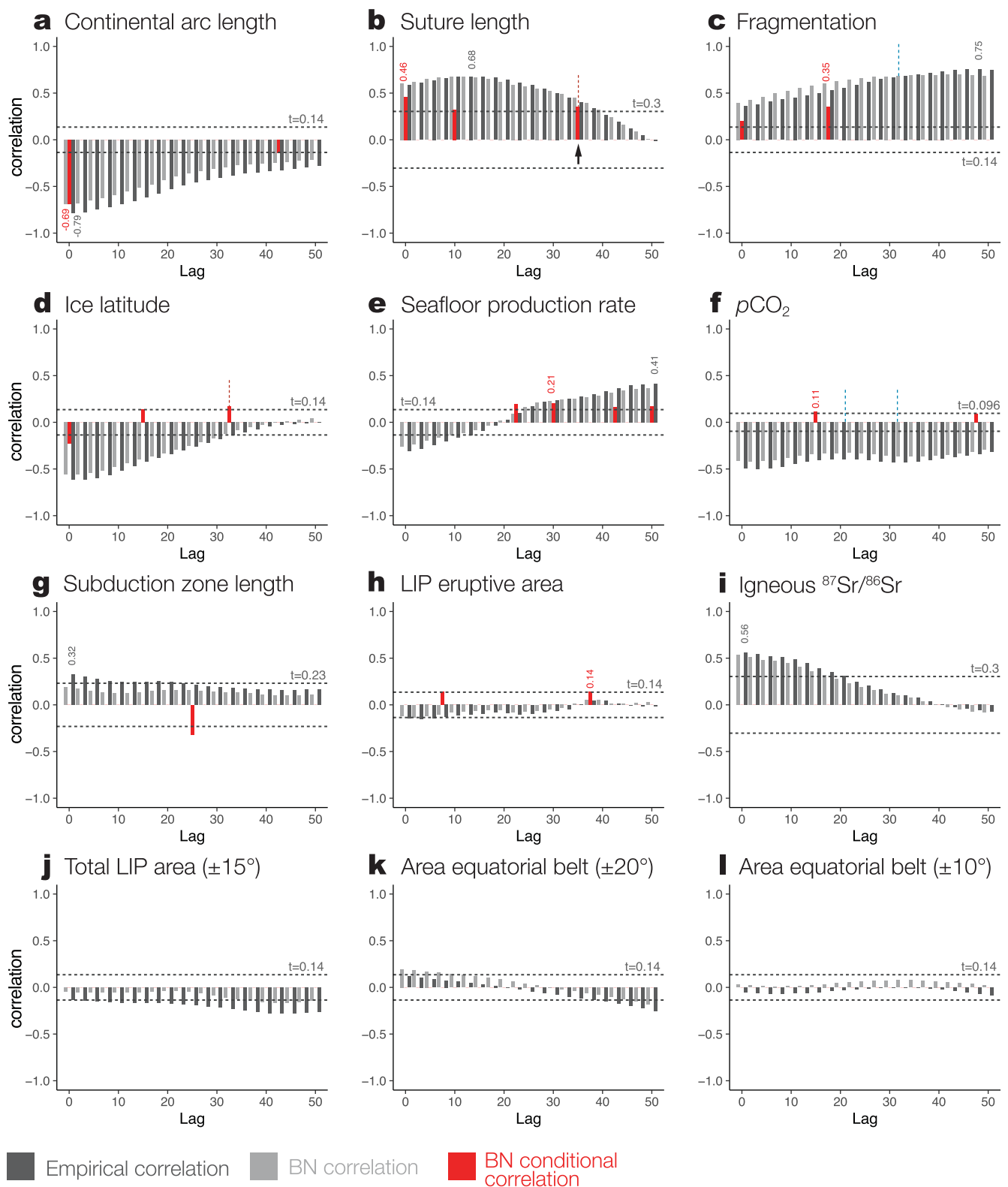
Extended Data Fig. 4 | The correlations of geologic processes with (^{87}Sr/^{86}Sr)$_{sw}$ and their time lags, using simulated input time series incorporating uncertainty estimates. Similar to Extended Data Fig. 3, the plots show the empirical rank correlations (C_{Emp}), Bayesian Network correlations (C_{BN}), and BN conditional rank correlations (C_{Cond}), at time lags from 0 to 50 Myr in 2.5 Myr intervals. The difference here is that the model incorporates all the input uncertainty distributions (shown in Extended Data Fig. 2, and Supplementary Data File S2). Note that including these uncertainty distributions does not cause any major changes in the strength of correlations, or the apparent response timescales. The main changes (those above the confidence interval [CI] threshold) are shown by the vertical dashed lines (red for gain, blue for loss of C_{Cond}); this includes an apparent weakening of the effects of atmospheric CO_2 (likely due to the large uncertainty in this variable; Extended Data Fig. 2). We note however that this is replaced by 'ice latitude'—a related proxy for climate state—at similar time lags. CI thresholds (dashed line, denoted t) are unchanged as these are estimates based on the resolution of the original input data.
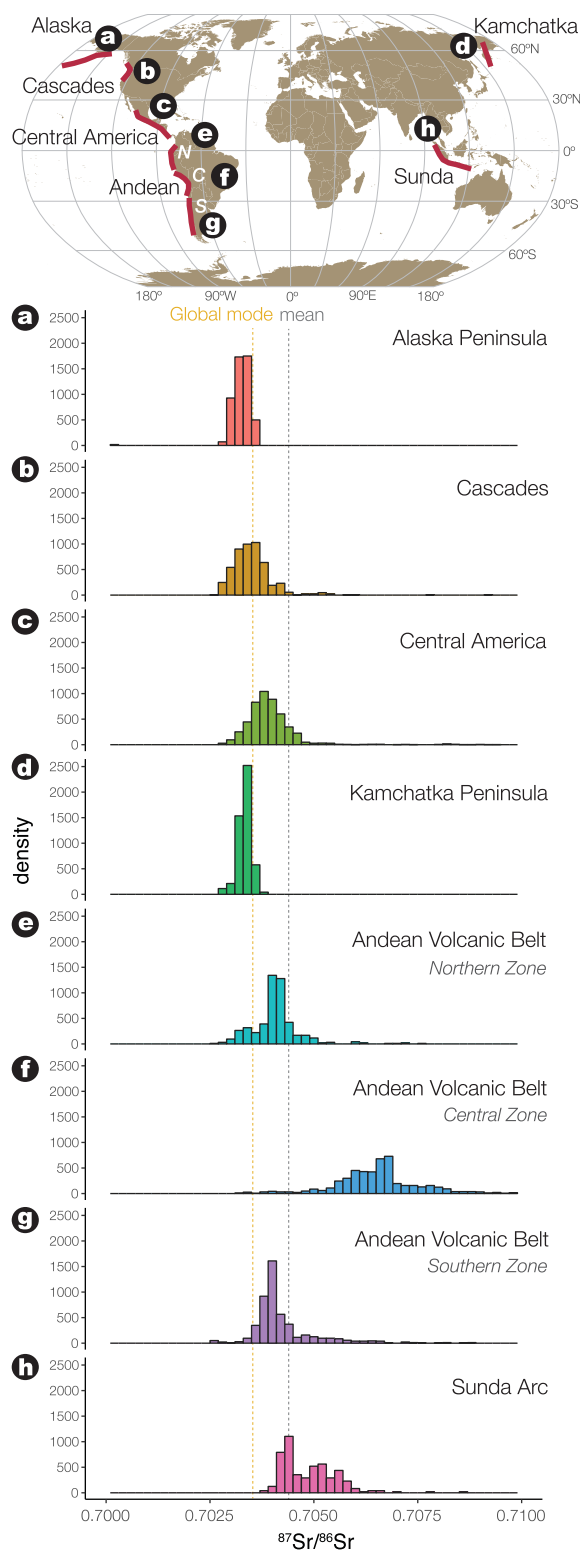
Extended Data Fig. 5 | Present-day global distribution of continental volcanic arcs, and their Sr isotope compositions. Map of continental volcanic arcs identified by Cao et al.[15]. The labels (a-h) correspond to the density histograms, which show the relative frequency of $^{87}Sr/^{86}Sr$ points for each arc from the EarthChem Library (earthchem.org). The mean and mode of the dataset (total N=5498) are represented by vertical dashed lines. Note that the relatively high $^{87}Sr/^{86}Sr$ compositions of the Central Zone of the Andean Belt can be explained by the presence of extremely thick crust in this region (>70 km) and a higher degree of crustal assimilation[66].
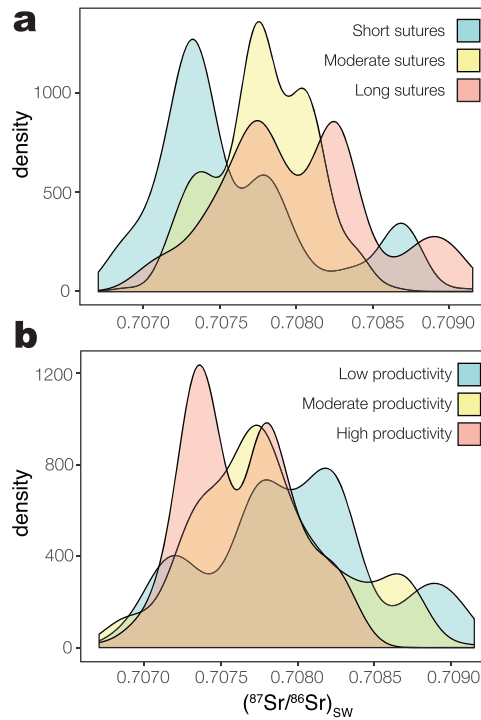
Extended Data Fig. 6 | Effects of suture zones and seafloor production rates on the strontium isotopic composition of seawater. Probability density for a, suture zone length[9], identifying short (<5,180 km), intermediate (5,180-9,730 km), and long (=9,730 km) suture zones (note that these divisions are approximately equal quantiles); and b, seafloor production rates, discriminating low (<3.96 km^2 yr^{-1}), moderate (3.96-4.95 km^2 yr^{-1}) and high (>4.95 km^2 yr^{-1}) production rates.
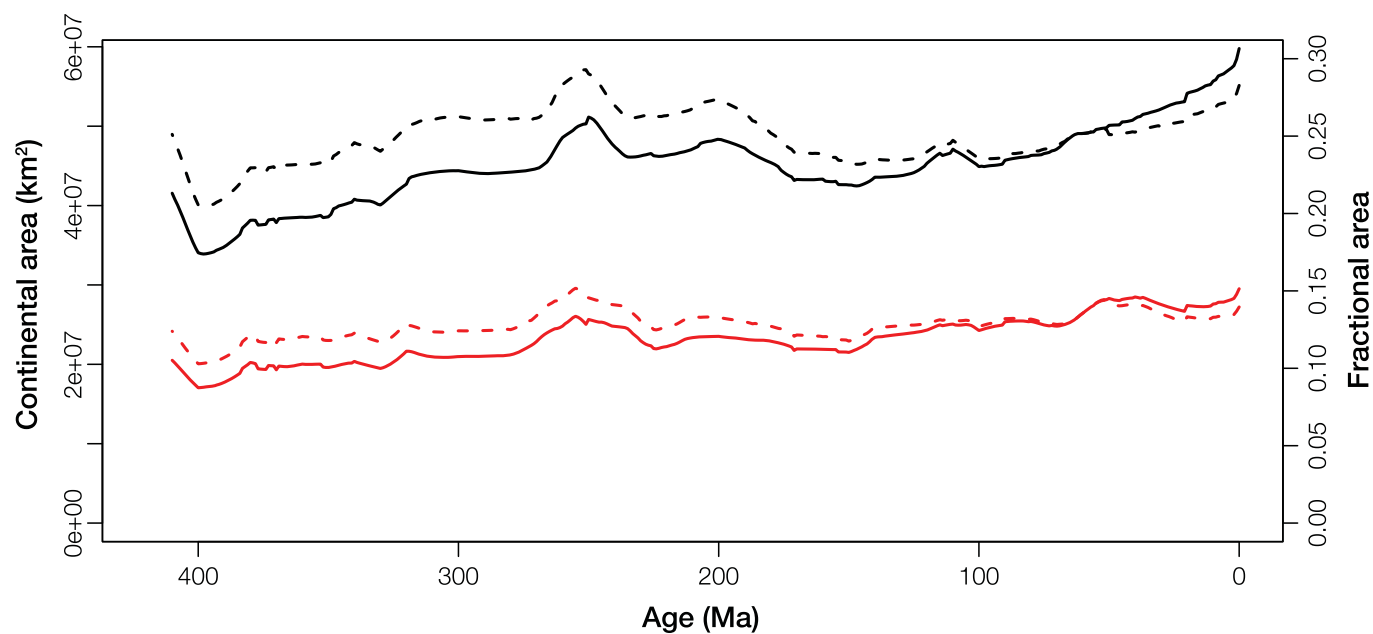
Extended Data Fig. 7 | Clustering of continents within the tropics since 400 Ma. Solid lines show the continental area within 20° (black) and 10° (red) of the equator through time, using the paleomagnetic reference frame of Domeier and Torsvik[67], as extracted from Matthews et al.[11]. The dashed lines show the fractional area (that is, area within the belt divided by the total crustal area) through time. The source data are provided in Supplementary Data File S1.
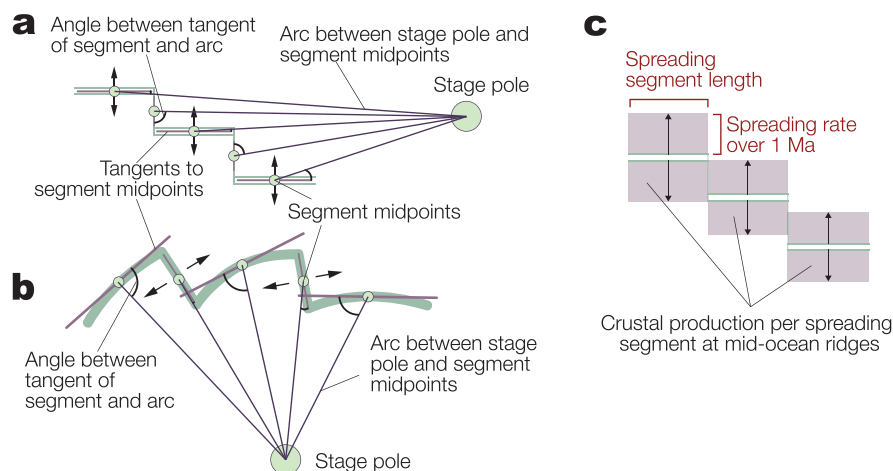
Extended Data Fig. 8 | Calculation of seafloor production at mid-ocean ridges. Diagram explaining the formal quantification of seafloor production rates (Methods). In GPlates, mid-ocean ridges contain both spreading and transform segments. a, and b, show how we distinguish these segments. Each mid-ocean ridge line is broken into separate segments. We take the mid-point of each segment and draw the tangent to it. In some cases this matches the segment quite well (for example, a) and in other cases the segment is more curved (for example, b). We then draw a great circle from the stage pole that describes the motion of one ridge flank from the other, to the mid-point of the segment. We then calculate the deviation angle between these two lines. As transform segments should form small circles around the stage pole, their deviation angle should be large, whilst the deviation angle for spreading segments should be small. We found 70° was a reasonable cut off, though in some locations where spreading is poorly constrained or very oblique, it does not work completely. Once we distinguished the spreading and transform segments, we extract the full spreading velocity of each segment c, and multiply this by the length of the ridge segment to calculate the crustal production.

Node	(a) Original input			(b) Simulated input		
	C_{Emp}	C_{BN}	C_{Cond}	C_{Emp}	C_{BN}	C_{Cond}
Continental Arc Length	**-0.787**	**-0.700**	**-0.700**	**-0.786**	**-0.690**	**-0.690**
Suture Zone Length	**0.592**	**0.606**	**0.468**	**0.587**	**0.603**	**0.460**
Ice Latitude	-0.719	-0.678	-0.299	-0.613	-0.561	-0.230
Fragmentation	0.374	0.408	0.214	0.358	0.395	0.198
LIP Eruptive Area Av 7.5 Myr	-0.110	-0.084	0.139	-0.130	-0.103	0.137
Suture Zone Length Av 10 Myr	**0.678**	**0.673**	**0.327**	**0.673**	**0.672**	**0.324**
PCO_2 Av 12.5 Myr	-0.496	-0.430	0.180	-0.424	-0.359	0.092
Fragmentation Av 15 Myr	**0.513**	**0.582**	**0.308**	**0.498**	**0.579**	**0.310**
PCO_2 Av 20 Myr	-0.457	-0.381	0.182	-0.398	-0.330	0.109
Seafloor Production Av 20 Myr	0.029	0.021	0.151	0.026	0.020	0.118
Subduction Length Av 22.5 Myr	0.238	0.177	-0.292	0.227	0.159	-0.301
Seafloor Production Av 27.5 Myr	**0.220**	**0.206**	**0.312**	**0.219**	**0.210**	**0.332**
Fragmentation Av 32.5 Myr	0.681	0.674	0.212	0.684	0.681	0.201
PCO_2 Av 32.5 Myr	-0.493	-0.429	0.136	-0.431	-0.365	0.019
Seafloor Production Av 40 Myr	0.319	0.265	0.168	0.334	0.285	0.211
Seafloor Production Av 47.5 Myr	0.391	0.343	0.216	0.409	0.358	0.212
PCO_2 Av 47.5 Myr	-0.380	-0.371	-0.110	-0.340	-0.314	-0.044
Continental Arc Length Av 50Myr	-0.267	-0.208	0.146	-0.278	-0.213	0.008

Extended Data Table 1 | Correlations for all nodes in our final Bayesian Network with $(^{87}Sr/^{86}Sr)_{sw}$. Note that C_{Emp} = Empirical Rank Correlation; C_{BN} = BN Rank Correlation; C_{Cond} = Conditional Rank Correlation; Av = Average value over a 2.5 Myr window, up to the given lag (in Myr); for example, LIP eruptive area Av 7.5 Myr is the correlation between Sr and the average LIP eruptive area over time $\geq$(t-7.5) Ma to time <(t-5) Myr (note that if this is not specified the interval is 0 Myr; that is no lag). Nodes with C_{Cond} greater than the 99 percent confidence interval threshold (CI_{thresh}, see the Methods for further details) were retained in the BN and are shown here. The reader is directed to Supplementary Data File S3 for the full table of correlations that includes nodes that were subsequently eliminated from the BN. Correlations calculated using (a) original inputs, and (b) simulated inputs (incorporating uncertainty distributions) are shown for comparison. To investigate how input uncertainty might affect the estimated correlations, we took the BN structure obtained using our original 'best estimate' data and recalculated all the network parameters using our new simulated data set. The resulting C_{Emp}, C_{BN} and C_{Cond} are shown in the last three columns. This shows that the dominant processes, that is, those nodes with the strongest influence (rows in bold), do not change significantly; and all nodes with the highest C_{Cond} remain highest within the simulated output.

Node	$(^{87}Sr/^{86}Sr)_{sw}$	$N(^{87}Sr/^{86}Sr)_{sw}$	Ign. $^{87}Sr/^{86}Sr$
Continental arc length	-0.787	-0.819	-0.704
Suture zone length	0.592	0.395	0.378
Ice latitudinal extent	-0.719	-0.561	-0.624
Land area, tropics (±20°)	0.134	-0.085	0.022
Land area, tropics (±10°)	-0.074	-0.409	-0.341
Fragmentation index	0.374	-0.007	-0.099
Subduction zone length	0.325	0.529	0.660
Seafloor production rates	-0.303	-0.282	-0.510
pCO_2	-0.571	-0.401	-0.225
LIP weatherable area (±15°)	-0.139	-0.535	-0.403
LIP eruptive area	-0.074	-0.341	-0.358
Igneous $^{87}Sr/^{86}Sr$	0.554	0.738	1.000
$N(^{87}Sr/^{86}Sr)_{sw}$	0.716	1.000	0.738
$(^{87}Sr/^{86}Sr)_{sw}$	1.000	0.716	0.554

Extended Data Table 2 | Empirical rank correlations (C_{Emp}) for $(^{87}Sr/^{86}Sr)_{sw}$, normalized $(^{87}Sr/^{86}Sr)_{sw}$, and $^{87}Sr/^{86}Sr$ of igneous (ign.) rocks[20], with all unlagged observables. Note that the data used to calculate the correlations C_{Emp} in this table span the interval from 1-360 Ma (that is, to allow a direct comparison with Extended Data Table 1), and that no time lags are included here.